Politecnico di Milano

SCHOOL OF INDUSTRIAL AND INFORMATION ENGINEERING

Master of Science – Engineering Physics

Evaluating the use of diffuse correlation spectroscopy for non destructive quality assessment of food

Supervisor

Prof. Alessandro Torricelli

Co-Supervisor

Ing. Caterina Amendola

Candidate

Hugo Harleston Aguirre – 940917

Academic Year 2020 – 2021

Acknowledgements

This work has been possible only due to the support, collaboration, and orientation of many people: teachers, friends, family. To mention them all here would not be possible, but I want to use this space to make a few special mentions.

First of all, I want to thank my supervisor, Professor Alessandro Torricelli, for giving me the opportunity of working on my thesis in the fNIRS Laboratory, and for his full support, which gave me the possibility to complete this work in time and form. I would also like to thank engineer Caterina Amendola, for her supervision, company, and patience during my stay at the laboratory. Thank you for your guidance.

My profound gratitude goes towards the close friends that I have made during my stay in Milan. To my roommate, Óscar, my flat mate, Luis, and my friends and neighbors: Joey, David, Marat, Inna, and Sara, thank you for your company and support throughout this adventure. May we have many more, together, in our future.

A very special mention goes out for Paulina, as our journey together through academic life began long ago in the Bachelor's degree, and by sheer coincidence continued again together here in Italy. Out of all of the universities in the world, we both chose this one for our Master's degree, without knowing that the other had done it too. Thank you for your never-ending support, and for the occasional wake-up call.

My thanks go as well to the usual people, the ones that are always there: Charlie, Poncho, Lydia, Joel, even when we are halfway across the world, I still feel your company and support very close to me.

Andrea, you arrived at the end of my adventure here and quickly became one of its main supporters. Your love and companionship have fueled the final leg of this journey. Thank you.

Finally, my deepest gratitude goes, as always, to my main pillar in life: my family. To my father, my mother, and my sister: everything I achieve is thanks to you, as everything I do always has a bit of you in it, because I am who I am thanks to you.

THANK YOU

Sommario

La necessità di tecniche mediche non invasive e a basso costo che generino una diagnosi di alta qualità è in aumento. Una di esse è la spettroscopia, in particolare, la spettroscopia a correlazione diffusa (DCS) e la spettroscopia risolta nel tempo (TRS), che sfruttano luce nel vicino infrarosso (NIRS), vengono spesso utilizzate per la loro capacità di monitorare il tessuto vivente e le sue proprierà ottiche ed emodinamiche. In questa tesi, un dispositivo ibrido che combina moduli DCS e TRS viene utilizzato per analizzare le proprietà ottiche e dinamiche (coefficienti di assorbimento e scattering e coefficiente di diffusione, rispettivamente) di diversi tipi di frutta. Poiché la frutta non è mai stata studiata prima con questo tipo di dispositivi, questo progetto vuole testare la possibilità di sfruttare queste tecniche per investigare le caratteristiche dei frutti. Mira anche a valutare quanto bene due diversi li teorici siano adatti ad analizzare i dati ottenuti. In particolare, nei modelli utilizzati si approssimano i frutti come mezzi omogenei semi-infiniti ed in un caso le particelle scatteranti si muovono di moto Browniano ed in un secondo caso una percentuale di elementi scatteranti sono statici. I risultati ottenuti sono messi a confronto e presentati.

I due obiettivi principali di questo lavoro sono quelli sopra menzionati:

- Valutare e studiare diversi tipi di frutta con il dispositivo ibrido DCS e TRS, per testare la validità dei risultati ottenuti. Per valutare la possibilità di utilizzo di queste tecniche su materiali di diversa composizione e rigidità, sono stati utilizzati anche fantocci appositamente progettati per avere caratteristiche simili a quelle dei tessuti viventi. La frutta viene scelta per questa analisi ipotizzando che il loro interno succoso possa assomigliare a tessuto vivente.
- Confronto di due diversi modelli teorici per stabilire quale di essi si adatta meglio alle misure effettuate e produce risultati migliori.

Dopo un'introduzione teorica nei primi capitoli, viene presentato il dispositivo utilizzato e vengono discussi i risultati sperimentali ottenuti sia per i fantocci che per il frutto. In generale, i risultati ottenuti per il frutto presentano un’elevata variabilità tra i tipi di frutta e anche tra le diverse misurazioni effettuate per lo stesso frutto. I risultati sono ulteriormente discussi alla fine di questo lavoro. Nel capitolo finale viene fornita una breve descrizione di possibili miglioramenti futuri.

Abstract

The need for non-invasive and low-cost medical techniques that generate a high-quality diagnosis is increasing. Spectroscopic techniques are particularly suitable in this field, particularly, Diffuse Correlation Spectroscopy (DCS) and Time Resolved Spectroscopy (TRS), exploit Near Infrared ligth (NIR) to monitor optical and hemodynamic properties of living tissues. In this thesis, a hybrid TRS and DCS device is used to analyze the optical and dynamical properties (absorption and scattering coefficients, and the diffusion coefficient, respectively) of different types of fruit. As fruit has never been studied before with this kind of devices, this project aims to test the possibility of using these techniques to evaluate fruit's characteristics. Moreover, it aims to evaluate how well two different theoretical models can evaluate and fit the obtained data. These two models approximate the fruits as semi-infinite homogeneous media and in one case all the scattering particles are approximated to move with Brownian motion, in the second model a percentage of the static background ones is taken into account. The results obtained with them were compared and presented here as well.

The two main objectives of this work are those mentioned above:

- Evaluate and study different types of fruit with the hybrid DCS and TRS device, to see how viable are the obtained results. In order to have a point of comparison, specially made phantoms that are engineered to have similar characteristics to those of living tissues, are used too. Fruit is chosen for this analysis because it is hypothesized that their juicy interior may resemble living tissue up to a certain point, and therefore the obtained results may be interesting to analyze.
- Compare two different theoretical models to see if any of them fits the data in a better way and yields better results in general.

After a theoretical introduction in the first chapters, the used device is introduced and the experimental results obtained for both the phantoms and the fruit are discussed. In general, the results obtained for the fruit show a remarkable variation between types of fruit or even between the different measurements made for the same fruit. This is further discussed at the end of this work. A brief outline for future improvements is given in the final chapter.

Table of Contents

Acknowledgements ..... **III**

Sommario ..... **V**

Abstract ..... **IX**

Table of Contents ..... **XI**

List of Figures ..... **XIII**

List of Tables ..... **XVII**

Chapter 1 Introduction **1**
1.1 Objectives 2
1.2 Outline 2

Chapter 2 Theoretical Background **5**
2.1 Diffuse Optics 6
2.1.1 Absorption 6
2.1.2 Scattering 7
2.1.3 Source-detector geometry 9
2.2 Radiative Transport Equation 9
2.2.1 Photon Diffusion Equation 10
2.3 Time-Resolved Reflectance Spectroscopy 11
2.4 Diffuse Correlation Spectroscopy 12
2.4.1 Autocorrelation Functions 13
2.5 Brownian Motion 14
2.5.1 Diffusion of the Temporal Correlation Function 15
2.5.2 Semi-Infinite Homogeneous Media 16
2.6 Autocorrelation Diffusion Equation With Static Background 17

Chapter 3 System Architecture **20**
3.1 DCS device 20
3.1.1 Light Injection and Detection 23
3.1.2 Injection Path 24
3.2 System Correlator and Multiple Tau Correlation Function 24
3.2.1 Linear Correlator 24
3.2.2 Multiple Tau Correlation Technique 26
3.3 TRS device 26
3.4 Sample Materials 27
3.4.1 Phantoms 28
3.4.2 Fruit 28

3.4.3 Probes 29

Chapter 4 Phantom Results 33
4.1 Epoxy phantoms 34
4.1.1 Phantom label: Epoxy_1 34
4.2 Silicon phantoms 38
4.2.1 Phantom label: Sylgard_1 38
4.3 Liquid phantom 43
4.4 Static background model implementation 46

Chapter 5 Fruit Results 52
5.1 Groups with different types of fruit 52
5.1.1 First set of measurements 53
5.1.2 Second set of measurements 64
5.2 Group of apples 73
5.2.1 Comparison between apples 73
5.2.2 Comparison between models 76

Chapter 6 Conclusions and Future Perspectives 79

Bibliography 81

List of Figures

Figure 2.1 - Graphical representation of the different scattering regimes [21]. 8
Figure 2.2 - Representation of each term of the RTE. (1) net flux of photons; (2) absorption losses; (3) scattering losses; (4) gain due to diffused photons; (5) source term [10, 11]..... 10
Figure 2.3 - Speckle pattern formed by the reflection of a laser beam on a rough surface [29]..... 13
Figure 2.4 - Schematic of the EBC in a semi-infinite geometry. An infinite surface, Σ, separates a diffusive medium with a refraction index n_{diff}, from a non-diffusive medium with a refraction index n. The real source is approximated by an isotropic one, located at a depth of $z_+ = l_{tr}$. A negative source located at $z_- = -2z_b - l_{tr} = -4AD - l_{tr}$ is taken into account. The dashed line located at $-z_b$ represents the extrapolated zero boundary surface. The dark arrows represent both the injection and detection points, separated from each other by a distance ρ..... 17
Figure 3.1 - Schematic representation of the DCS module of the hybrid-device [42]. 20
Figure 3.2 - Hybrid DCS and TRS device during measurements on the forearm [42]. 21
Figure 3.3 - Internal structure of the DCS device [42]..... 22
Figure 3.4 - Multiple tau correlation technique. Square cells represent the duration of the sampling time, while the gray cells represent the redundant information coming from the first channels [44]. 26
Figure 3.5 - TRS device schematic diagram [8]..... 27
Figure 3.6 - (a) Lateral view of the 3-D probe. (b) Dimensions of the probe (cm), where the green boxes represent the DCS injection and detection points and the orange ones represent the same for the TRS part. (c) Probe utilized in an in vivo measurement [42]. (d) Probe with an interfiber distance of 2 cm used for the majority of the measurements done in this thesis.....30
Figure 4.1 - Curves obtained, both g1 and g2 (blue) for an epoxy phantom with different acquisition times of 1 second (top), 5 seconds (middle) and 10 seconds (below). Their respective fits are shown in red. 35
Figure 4.2 - Values obtained for D_B and β in different acquisition times of 1, 5, and 10 seconds for an epoxy phantom. 36
Figure 4.3 - All of the curves obtained for the epoxy phantom are presented here (1 second case above, 10 second case below). The g_1 curves begin relatively equal to each other while their decay varies a lot. For g_2, the curves have varied ranges in general, and not only in a particular area as g_1 38
Figure 4.4 - Curves obtained, both g1 and g2 (blue) for a silicon phantom with different acquisition times of 1 second (top), 5 seconds (middle) and 10 seconds (below). Their respective fits are shown in red. 40
Figure 4.5 - Values obtained for D_B and β in different acquisition times of 1, 5, and 10 seconds for a silicon phantom 41
Figure 4.6 - All of the curves obtained for the silicon phantom are presented here (1 second case above, 10 second case below). The g_1 curves begin relatively equal to each other while their decay

considerably varies. For g_2, the curves have varied ranges in general, but not as varied as in figure 4.3 42
Figure 4.7 - Curves obtained, both g1 and g2 (blue) for a liquid phantom with different acquisition times of 1 second (top), 5 seconds (middle) and 10 seconds (below). Their respective fits are shown in red 44
Figure 4.8 - Values obtained for D_B and β in different acquisition times of 1, 5, and 10 seconds for the liquid phantom. 45
Figure 4.9 - All of the curves obtained for the liquid phantom are presented here (1 second case above, 10 second case below). The g_1 curves can be seen to overlap each other almost perfectly, with variations both at the beginning and the end of the curves. For g_2, the same behaviour can be noticed, with the exception that the curves overlap also very well at the end. When going from 1 second to 10 seconds, this behaviour can be seen even more notoriously 46
Figure 4.10 - Comparison between the new model implementation discussed in [41] (below) and the results obtained replicating the model in this work (above). All of the values utilized were the same as in [41]. Only two curves were replicated (their colors are the same in both figures) due to those being the only ones that utilized Brownian motion in [41], which is the motion used here. The other curves in the figure below are of no interest to this work. The graph depicted below has been directly obtained from [41]. 47
Figure 4.11 - A comparison between the classical model and the new model is shown here. The classical model (above) is compared against the new model with two different values for P_m: 0,025 (middle) and 0.07 (below). 49
Figure 4.12 - Values obtained for D_B and β in both the classical and new models, with different values for P_m. Even though the behaviour of the parameters is the same, the values for D_B change between models and also for different values of P_m. On the other hand, the β coefficient seems to remain unchanged. 50
Figure 5.1 - Comparison between the curves obtained for a lime with two different interfiber distances: 1 cm (above) and 2.5 cm (below). 54
Figure 5.2 - Values for the diffusion coefficient of a lime obtained for two interfiber distances (in cm). 55
Figure 5.3 - Comparison between the curves obtained for an orange with two different interfiber distances: 1 cm (above) and 2.5 cm (below). 57
Figure 5.4 - Values for the diffusion coefficient of an orange obtained for two interfiber distances (in cm). 58
Figure 5.5 - Comparison between the curves obtained for a tangerine with two different interfiber distances: 1 cm (above) and 2.5 cm (below). 59
Figure 5.6 - Values for the diffusion coefficient of a tangerine obtained for two interfiber distances (in cm). 60
Figure 5.7 - Comparison between the curves obtained for a tomato with two different interfiber distances: 1 cm (above) and 2.5 cm (below). 62
Figure 5.8 - Values for the diffusion coefficient of a tomato obtained for two interfiber distances (in cm). 63
Figure 5.9 - Fitting curves obtained for a tomato without peel at different points in time. P_m value = 0.025. 65
Figure 5.10 - Fitting curves obtained for an orange (with peel) for different acquisition times of 1, 5, and 10 seconds respectively. P_m value = 0.025. 67

Figure 5.11 - Fitting curves obtained for an aubergine (without peel) for different acquisition times of 1, 5, and 10 seconds respectively. P_m value = 0.025. 68
Figure 5.12 - Comparison between the values obtained for the diffusion coefficient of an orange with peel for different values of P_m. 69
Figure 5.13 - Diffusion coefficient obtained for different apples with the classical model. The first three apples were of the same type, while apples 4 and 5 were different to the first ones, and between them. 75
Figure 5.14 - Curves obtained for the same apple with the two different models and two different values of P_m. Their fitting is depicted in red. 77
Figure 5.15 - Diffusion coefficient values obtained for the same apple, but with the two different models and also two different values for P_m in the new model case. 78

List of Tables

Table 4.1 - Average value and standard deviation of both D_B and β obtained for an epoxy phantom 36
Table 4.2 - Average value and standard deviation of both D_B and β obtained for the silicon phantom 41
Table 4.3 - Average value and standard deviation of both D_B and β obtained for the liquid phantom 45
Table 4.4 - Average value and standard deviation of both D_B and β obtained for the silicon phantom and for two different models 51
Table 5.1 - Average value and standard deviation of both D_B and β obtained for a lime, using two different interfiber distances 55
Table 5.2 - Average value and standard deviation of both D_B and β obtained for an orange, using two different interfiber distances 58
Table 5.3 - Average value and standard deviation of both D_B and β obtained for a tangerine, using two different interfiber distances. 61
Table 5.4 - Average value and standard deviation of both D_B and β obtained for a tomato, using two different interfiber distances 63
Table 5.5 - Average value and standard deviation of both D_B and β obtained for the different fruits analyzed in this section, with and without peel 70
Table 5.6 - Average value and standard deviation of both D_B and β obtained for five different apples. 75

Chapter 1
Introduction

One of the main characteristics that have allowed us to grow as human beings is our capacity to be curious, study, and try to understand the world that surrounds us. One of the ways in which we do it is by gathering samples of one of its parts and analyze them separately from their origin. Sometimes, this also means that the samples must be destroyed in the process, or at least suffer considerable damage that renders them useless in the future. Thus, a non-invasive analysis of the world becomes of great importance to many fields of study.

In living beings, for example, one technique that has been used for this type of studies is Diffuse Correlation Spectroscopy (DCS) [1]. Particularly, DCS has been utilized to monitor microvascular blood flow, which has led to improvements in creating a personalized diagnosis for brain injury patients [2], and even improving the outcome of said patients by analyzing their blood flow and oxygen utilization in real time, allowing doctors to elaborate a better treatment for them [3]. There are many other studies that utilize the DCS technique to perform non-invasive analysis in patients, such as applying the technique in new born babies, which have thinner extracerebral layers than adults, allowing for a better reproducibility of the obtained results [5].

There are many other forms of studying cerebral hemodynamics, such as Single Photon Emission Computed Tomography (SPECT) [14] or Magnetic Resonance Imaging (MRI) [15]. Such techniques can be expensive, bulky, involve transporting patients, are in general complicated to apply, and some of them are even invasive. Therefore, having access to a device that can continuously perform non-invasive analysis, is affordable, and can be easily available for the patient's use, is of great importance [4]. Such devices are under development, and some of them have already been used in actual studies. For example, there is a device that combines both DCS and near-infrared spectroscopy (NIRS) to monitor the newborn brain [6,7]. Another system specialized in brain and muscle hemodynamic monitoring is also already in use [8]. In this thesis, one of said devices has been utilized to obtain data from different mediums, which then has been inserted into a couple of analytical models to test how well they process said results.

As mentioned in the last paragraph, DCS and NIRS have been combined to study living tissue in a non-invasive way. NIRS is utilized because near-infrared light (with wavelengths in a range between 600nm to 1000nm) can easily penetrate human tissue, which in this range

presents a scattering coefficient that is two orders of magnitude greater than its absorption coefficient [9]. In particular, time-resolved NIRS (TRS) allows the study of the scattering and absorbing information of the tissue separately, which leads to obtaining the values of the coefficients related to each of these processes. Said coefficients can then be utilized along with the DCS technique to obtain further information regarding the diffusion coefficient of the examined tissue, or fluid [10,11]. Research regarding these studies can be found consulting [6-8], while other research utilizing these techniques has been done to study functional activation of the brain while performing cognitive tasks [12] and breast cancer tumors [13].

1.1 Objectives

This thesis work has two main objectives.

- Probe a hybrid DCS and TRS device in different types of fruit and phantoms to study the reliability of its results. Mainly, fruit has not been analyzed before with a device of this nature. Hypothesizing that the juicy, pulpy interior of different fruits has conditions that may be like those of human tissue, analyzing the results obtained with the DCS device may yield interesting conclusions. Due to the different composition of the fruits, measurements were also performed on phantoms with different hardness and stable optical and dynamic properties. Particularly, epoxy and silicon phantoms were used, in order to analyze if they could be distinguished through the DCS technique.
- Compare two different analytical models to find if any of them fits the obtained data in a better way. Both models are discussed in the theoretical part of this work, while the results obtained with them are compared in chapter four. Finding a better suited model would improve the device's ability to obtain more reliable data.

1.2 Outline

Besides this first introductory chapter, this thesis includes five more chapters.

- Chapter 2 is dedicated to giving a theoretical background regarding DCS. To do so, diffuse optics focused on light propagation in a turbid media are disccused from a physical point of view. Radiative transport theory is mentioned to introduce a description of light's optical properties and the photon diffusion equation. From here, the thesis builds up into the physics of photon propagation in diffusive media, which leads to the theory that describes the DCS technique. A brief introduction will also be made about TRS. Finally, a description of the analytical models utilized to process the results will be given.

- Chapter 3 focuses on the device utilized and its architecture. The TRS system is mentioned, while the main discussion revolves around the DCS system. The optical and electronic components of the device, the light injection and detection system, and the role of the correlator will all be discussed here. Afterwards, a brief description of the materials analyzed with the device (both phantoms and fruit) is given.
- Chapter 4 presents the experimental results obtained for the phantoms with the device and their analysis. Results were obtained for different types of phantoms, made of synthetic materials, that have similar characteristics to human tissue. A comparison between the results obtained with different analytic models is presented here.
- Chapter 5 presents the experimental results obtained for the fruit with the device and their analysis. Results were obtained for different types and groups of fruits, in order to see, first, how well both utilized models fit the data, and also how the results change between different types of fruit that have, therefore, different characteristics overall. Another comparison between the results obtained with different analytic models is also presented here.
- Chapter 6 concludes the work and briefly discusses the possible future development of these studies.

Chapter 2
Theoretical Background

To be able to speak about DCS, one must first define the basic concepts behind it. Mainly, how light propagates through a medium which, in this case, is considered turbid. This propagation's theory builds up from the dual nature of light as a particle and as an electromagnetic wave, focusing on the first one, and considers how photons interact with different particles of matter as they travel through it. The two main processes that describe this interaction are absorption and scattering. By discussing how these processes function, one can begin to grasp the basic principles of the Radiative Transport Theory, from which the Radiative Transport Equation stems. By considering certain approximations to this equation, the Photon Diffusion Equation can be defined. An analysis of this equation can be done to obtain information about the optical properties of the medium through which light is propagating.

Once all the above is done, both TRS and DCS can be discussed. The first one, TRS, will only be briefly mentioned in this chapter, because it is not included in the scope of this project, but it is important to obtain information that can afterwards be combined with a DCS setup, which will be further discussed here. One of the key concepts regarding DCS, the autocorrelation functions of the electric field and its intensity, will be introduced. A parameter that is of interest in these types of studies is the diffusion coefficient of the analyzed medium, which can be obtained through the analysis of the previously mentioned equations. To understand the parameter in profundity, a section in this chapter is dedicated to Brownian Motion Theory, from which said coefficient emerges. In this thesis, the mediums under study have been considered semi-infinite and homogeneous. Therefore, there will also be a discussion about such characteristics here.

Finally, an alternative way of obtaining the autocorrelation diffusion equations previously mentioned will be introduced, in which a static background is considered, thus changing the general form of the expressions for both autocorrelation functions. The results obtained during this work will be analyzed in later chapters with both sets of equations in order to compare them, and determine if one is better than the other in the studies realized here.

2.1 Diffuse Optics

Light propagates through a turbid media in the diffusive regime when the propagation occurs mainly due to the scattering process, in which a photon can undergo multiple scattering events before its detection [16]. Diffuse optics is the field of physics where these phenomena are studied.

A photon undergoes a scattering event whenever it changes its trajectory after interacting with a particle of matter (a molecule, an atom, etc.). But sometimes, when a photon interacts with matter, it transfers all of its energy to it instead of changing direction and continuing its path. Whenever this happens, the photon is said to be absorbed by the medium. Both of these processes have therefore a major influence in the propagation of light through turbid media, and so they are discussed in the following sections.

2.1.1 Absorption

A photon can transfer its energy to an electron, leading it into an excited state, and provoking it to either release heat while returning to its ground state, or to emit another photon with a different wavelength, before returning to its ground state [16]. In any of these cases, the original photon is said to be absorbed by the matter with which it interacted.

The absorption coefficient, μ_a, is defined as the probability of a photon being absorbed per unit path length. In a highly absorbing medium, the intensity of light, I, absorbed after travelling a certain distance, z, through it, will be given by the Lambert-Beer Law [17]:

$$\mathrm{I(z)} = I_0 e^{-\mu_a z}. \tag{2.1.1}$$

Here, I_0, is light's intensity at a distance of $z = 0$, and the direction of the propagation of light is considered to be parallel to z.

The absorption coefficient strongly depends on both the characteristics of the medium and the wavelength of the interacting light. In a highly absorbing medium, with N non-interacting absorbers, μ_a can be written as:

$$\mu_a(\lambda) = \sum_{i=1}^{N} \varepsilon_i(\lambda) c_i. \tag{2.2.2}$$

The dependance on the wavelength, λ, can be seen through ε_i, which represents the molar extinction coefficient of an absorber, while c_i is the concentration of the i_{th} absorber [17,6].

Inverting μ_a leads to the average absorption length, l_a, which is the mean length that a photon will travel in a medium before being absorbed.

2.1.2 Scattering

The refractive index, *n*, of a medium is defined as the quotient between the speed of light in the vacuum, *c*, and the phase velocity of light in the medium, *v* [19]:

$$\mathrm{n} = \frac{c}{v}. \tag{2.3.3}$$

If the scattering process, as mentioned before, involves the change of direction of a photon after interacting with a particle from the medium, then its phase velocity in said medium is not constant, and therefore one can say that the refractive index here is not constant. This is due to structural inhomogeneities in the medium [17]. Scattering can be both elastic (when the energy of the photon before and after the scattering event remains unchanged) and inelastic (when said energy changes). This is the same as the concept of elastic and inelastic collisions [20].

The probability of a photon scattering in a medium per unit of length is called the scattering coefficient, μ_s. The reciprocal of this factor is called *ls*, and represents the average distance traveled by a photon before it undergoes a scattering event [17]. When the optical thickness of the medium (i.e., the product of the scattering coefficient times the thickness of the medium) is considerably smaller than 1, the scattering process can be modeled in the same way as the absorption process:

$$\mathrm{I(z)} = I_0 e^{-\mu_s z}. \tag{2.4.4}$$

However, this is not always the case, and a deeper analysis should be made when the scattering coefficient does not suffice that condition. One example in which μ_s is close to, or even larger than 1, is biological tissue. In this case, the coefficient value oscillates around 100 cm^{-1}, so a different approach must be taken to understand the scattering processes that occur here.

To do so, two approximations can be taken into account, where the ratio between the wavelength, λ, of the incident light and the diameter, *d,* of the scatterers is evaluated.

1. Light is diffused in a homogeneous way when $\frac{\lambda}{d} \gg 1$. This is called the Rayleigh regime.
2. Light is diffused inhomogeneously and mainly in a forward direction, when $\frac{\lambda}{d} \approx 1$, which is the Mie regime. Here, the larger the particle, the more concentrated the scattering will be in the forward direction (figure 2.1).

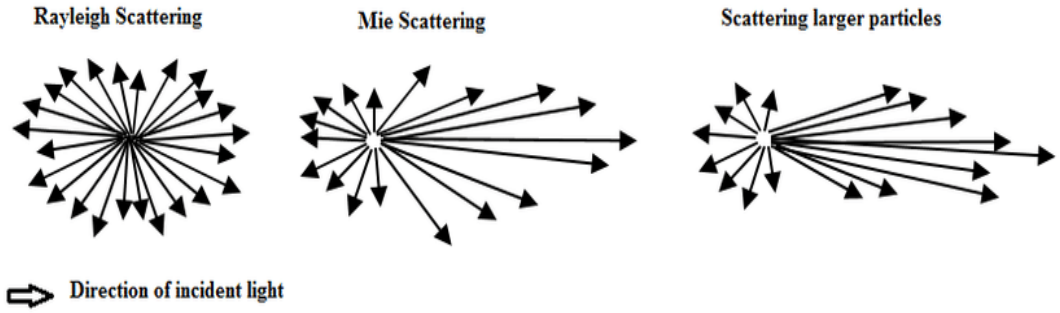

Figure 2.1 – Graphical representation of the different scattering regimes [21].

In Figure 2.1 it is possible to see that the scattering events in the Rayleigh regime are mostly isotropic, and therefore, the direction of the photon after undergoing scattering is randomized. On the other hand, in the Mie regime this randomization is not immediate, but after a photon is scattered a certain number of times, the memory about its initial propagation direction is lost. An interesting way of interpreting this is by looking at the probability that a photon initially traveling in a direction $\bar{r}$ will take the $\bar{s}$ direction after scattering. This probability will be a function of both the photon's direction before and after scattering takes place, and it is called the *phase scattering function,* $p(\bar{r}, \bar{s})$[16]. In an isotropic medium this function will be only dependant on the scattering angle, θ, between both directions, and so it can be rewritten as $p(\theta)$.

If anisotropy is present, then one way to measure it is through the anisotropy factor, *g,* which is defined as the average value of the cosine of the scattering angle [23]:

$$\mathrm{g} = \int_{4\pi} \cos(\theta)\, p(\bar{r}, \bar{s}) d\Omega = 2\pi \int_0^{\pi} \cos(\theta)\, p(\theta) \sin(\theta)\, d\theta. \tag{2.5.5}$$

For isotropic scattering, $g = 0$, while $\mathrm{g} < 0$ represents backward scattering (which is whenever the scattering angle is between 0 and -180º) and $\mathrm{g} > 0$ means forward scattering (when the scattering angle is between 0 and 180º) [22].

By considering this factor, one can define the reduced scattering coefficient, μ_s':

$$\mu_s' = (1 - \mathrm{g})\mu_s. \tag{2.6.6}$$

As with the other coefficients discussed here so far, the reciprocal of the reduced scattering coefficient will also represent a distance, which in this case is called the transport mean free path, and is the average distance traveled by a photon before the information about its initial propagation is completely lost, thus becoming random [24].

2.1.3 Source – Detector Geometry

During the experiments realized in this thesis, a particular geometrical setup was used for the source and detector of the photons. In this setup, called reflectance setup, both the source and detector were placed on the same side of the tissue under evaluation, at varying distances from each other. Here, once photons are injected from their source into the tissue, they will undergo several scattering events before arriving at the detector. Some will be absorbed by the tissue and will be considered lost. The scattered photons, though, can take many different paths to arrive to the detector, which also means enduring a different number of scattering events. The information obtained from different depths of the tissue will vary with the distance between the source and the detector. In steady-state (CW), the longer this distance, the more information is obtained from deeper layers of the tissue, while the shorter the distance, information from upper layers is obtained [11].

Depth sensitivity becomes then an important issue when working with non-invasive techniques like the ones used in this work. Having a good control over the depth sensitivity of the device determines how well one can evaluate the information obtained from the detector. For example, it has been demonstrated that it increases the accuracy in tumor identification and discrimination in optical mammography [25].

2.2 Radiative Transport Equation

The study of light propagation through space has been widely studied, and different approaches can be found to understand it. One of them is the Radiative Transport Theory, from which the Radiative Transport Equation (RTE) is derived. This equation represents a mathematical expression of the energy transferred as electromagnetic radiation. The three main processes that constitute this phenomenon are emission, absorption, and scattering [26]. In order to write the RTE, the problem needs to be localized in a finite volume inside the medium which will be studied, so that the energy balance can be imposed there [27].

Following the steps in [16], the RTE is built up in terms of the radiance, which they define as the average power measured per unit area and unit solid angle oriented in the $\bar{s}$ direction. It is measured at the position $\bar{r}$, and at time *t*, and it is denoted as $I(\bar{r}, \bar{s}, t)$. In terms of *I,* the RTE can be written as:

$$\frac{1}{v}\frac{\partial \mathrm{I}(\bar{r},\bar{s},\mathrm{t})}{\partial t} = -\nabla\big(\bar{s}I(\bar{r},\bar{s},\mathrm{t})\big) - (\mu_a + \mu_s)I(\bar{r},\bar{s},\mathrm{t}) + \mu_s \int_{4\pi} \rho(\bar{s},\bar{s}')I(\bar{r},\bar{s}',\mathrm{t})d\Omega' + \epsilon(\bar{r},\bar{s},\mathrm{t}). \tag{2.2.1}$$

The four terms in eq. 2.1.7 are further commented in the following, and their representation can be seen in figure 2.2:

- $-\nabla\left(\bar{s}I(\bar{r},\bar{s},\mathrm{t})\right)$ refers to the net flux of energy propagating in the $\bar{s}$ direction. The negative symbol of the radiance means that it is increasing inside the volume where it is evaluated. This is equivalent to say that photons are moving from a high-density region to a low-density region in the medium.
- $-(\mu_a+\mu_s)I(\bar{r},\bar{s},\mathrm{t})$ has to do with the losses sustained from absorption and scattering inside the volume.
- $\mu_s\int_{4\pi}\rho(\bar{s},\bar{s}')I(\bar{r},\bar{s}',\mathrm{t})d\Omega'$ on the other hand, represents the gain that comes from photons scattering from a direction $\bar{s}'$ into the direction $\bar{s}$.
- $\epsilon(\bar{r},\bar{s},\mathrm{t})$ is the gain that comes from any light source that is present inside the medium.

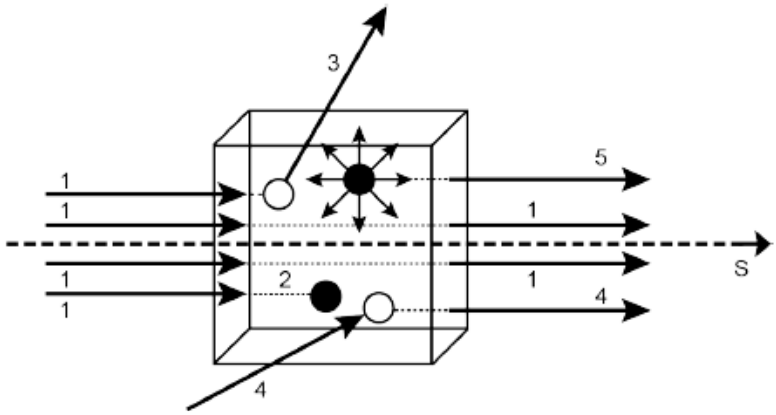

Figure 2.2 – Representation of each term of the RTE. (1) net flux of photons; (2) absorption losses; (3) scattering losses; (4) gain due to diffused photons; (5) source term [10, 11].

The derivation and solutions of the RTE are quite complicated, and in general, Radiative Transport Theory is out of the scope of this thesis, but it can be found in many important works such as [16, 26, 27]. The basic principles and the RTE equation mentioned here are meant to provide a brief introduction so that the Photon Diffusion Equation can be mentioned with more clarity in the following section.

2.2.1 Photon Diffusion Equation

By assuming certain approximations, the RTE can be reduced to the Photon Diffusion Equation (PDE). These approximations and in general the underlying theory regarding this section are stated and discussed in profundity in [16].

First, the radiance inside a diffusive medium is considered as isotropic. Therefore, it can be approximated with a series expansion in spherical harmonics and considering the first two terms of said expansion:

$$\mathrm{I}(\bar{r},\bar{s},\mathrm{t}) = \frac{1}{4\pi}\Phi(\bar{r},t) + \frac{3}{4\pi}\bar{J}(\bar{r},t)\bar{s}. \tag{2.2.2}$$

Here, $\Phi(\bar{r},t)$ represents the integral of the radiance over the solid angle, and is called the *fluence rate*. $\bar{J}(\bar{r},t)$ is the photon flux vector, and can be rewritten as $\bar{J}(\bar{r},t) = \int_{4\pi}\bar{s}I(\bar{r},t)d\Omega$.

Secondly, one can consider the variation of $\bar{J}(\bar{r},t)$ over a time interval $\Delta t = \frac{1}{v\mu_s}$ is negligible compared with its module. This can be expressed as:

$$\frac{1}{v\mu\prime_s}\left|\frac{\partial\bar{J}(\bar{r},\bar{t})}{\partial t}\right| \ll |\bar{J}(\bar{r},\bar{t})|. \tag{2.2.2}$$

Remembering that a diffusive media is that one in which $\mu_s' \gg \mu_a$, and taking this into consideration along with both previously made assumptions, the RTE can be simplified and rewritten as de PDE:

$$D\nabla^2\varphi(\bar{r},t) - v\mu_a\varphi(\bar{r},t) + vS(\bar{r},t) = \frac{\partial\varphi(\bar{r},t)}{\partial t}. \tag{2.2.3}$$

In this equation, D is the diffusion coefficient, which in a homogeneous medium is assumed to be space invariant, and is expressed as: $D = \frac{v}{3(\mu_s'+\mu_a)} \approx \frac{v}{3\mu_s\prime}$. The source term is $S(\bar{r},t)$. To find the general solution for the PDE, coherent boundary conditions must be taken into account, which will lead to the definition of some constant values that will take part of the solution. This is due to the nature of the PDE being a partial differential equation of the fluence rate.

2.3 Time-Resolved Reflectance Spectroscopy

The building blocks of Time-Resolved Spectroscopy (TRS) are laser pulses that last no more than few hundredths of picoseconds. By utilizing these pulses in a reflectance setup as the one discussed in 2.1.3, one can obtain a curve representing the temporal profile of the detected photons that come back from the tissue. Depending on the optical properties, mainly absorption and scattering, of the tissue, the curves that are obtained will change. They can be broadened, delayed, or attenuated. In particular, scattering will shift the peak of the curve, while absorption will affect the slope of the pulse's tail. These different effects of each

property on the pulse will allow to study them separately, and obtain information about both the absorption and the scattering coefficients of the studied tissue.

In order test the technique, phantoms of different materials were specifically made to resemble living tissue and, it was assumed that they were semi-infinite homogeneous media. This has been done because, for a delta-shaped pulse source, and with the correct boundary conditions in the interface between the tissue and air, the PDE (equation 2.2.3) can be solved, allowing one to write the curve representing the number of backscattered photons per unit time and unit area at a distance ρ, $R(\rho, t)$, as [16, 28]:

$$R(\rho,t) = \frac{v}{2A}\left(\frac{1}{4\pi Dt}\right) exp\left(-\frac{\rho^2}{4Dt} - \mu_a vt\right)\left[exp\left(-\frac{z_+^2}{4Dt}\right) - exp\left(\frac{z_-^2}{4Dt}\right)\right]. \quad (2.3.1)$$

In this equation, v is light's velocity in the medium, $A = \frac{1+R_{eff}}{1-R_{eff}}$, with $R_{eff}$the effective refraction coefficient, which accounts for the mismatch between the refractive indexes of both air and tissue at their interface, and ρ is the so called interfiber distance, which is the distance between the source and the detector. Furthermore, $z_+ = l_{tr}$, and $z_- = -4AD - l_{tr}$, represent (respectively) the depth of the tissue at which the scattered photons enter a random regime and some fictitious negative sources placed outside the tissue that are necessary to impose one of the boundary conditions, called the Extrapolated-zero Boundary Condition (EBC).

Equation (2.3.1) represents the response of the system interacting with a delta-shaped pulse. It can then be noticed that it does not consider the finite width of said pulse. So, to obtain the complete reflectance of the system, $\hat{R}(\rho, t)$, equation (2.3.1) needs to be convoluted with the real shape of the pulse that is referred to the instrument response function, $IRF(t)$:

$$\hat{R}(\rho,t) = R(\rho,t) * IRF(t). \quad (2.3.1)$$

The experimental curve made with the obtained data can then be fitted with this model to extract the value of both the absorption and scattering coefficients separately. This information is then utilized for the DCS analysis, which is discussed in the following section.

2.4 Diffuse Correlation Spectroscopy

When a spatially coherent laser beam reflects off of a rough surface, a granular pattern with bright and dark spots can be observed. This is known as a *speckle* pattern (Figure 2.3).

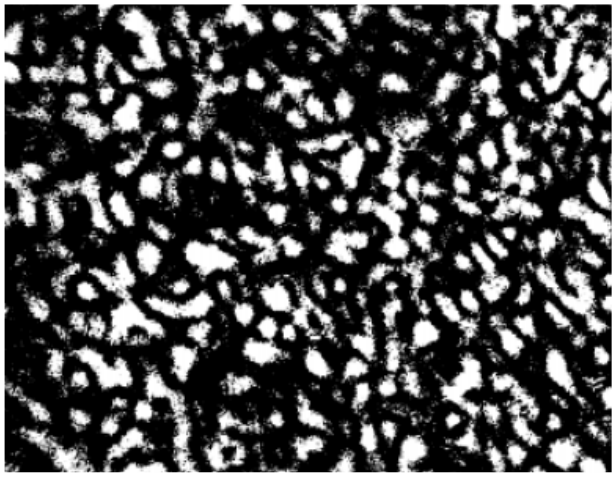

Figure 2.3 – Speckle pattern formed by the reflection of a laser beam on a rough surface [29].

What happens is that, due to the irregularities on the rough surface, different components of the beam will be reflected at different depths or points in the surface, leading them to follow different optical paths, and thus provoking interference between them. This interference can be destructive, constructive, or an in-between, which leads to the generation of a speckle pattern as seen in Figure 2.3 [30, 31]. This phenomenon can also be observed when light travels through turbid media [31].

In the case of biological tissue, the speckle pattern that generates when a laser beam (also spatially coherent) is reflected on it will fluctuate with time. These fluctuations are due to the moving nature of the scatterers [32].

Diffuse Correlation Spectroscopy (DCS) focuses on studying these temporal fluctuations of the intensity in the speckle pattern. By doing so, information about the motion of the scatterer can be retrieved. To further understand what has been mentioned here, the theory behind DCS will be discussed in the following sections.

2.4.1 Autocorrelation Functions

DCS is able to analyze the temporal fluctuations in the intensity of a speckle pattern through two functions that represent the autocorrelation of the electric field, $\bar{E}$, and the intensity, I. The first one is called G_1 and is given by:

$$G_1(\bar{r},\tau) = \langle \bar{E}^*(\bar{r},t)\bar{E}(\bar{r},t+\tau)\rangle = \lim_{T\to\infty}\frac{1}{T}\int_{-T/2}^{T/2}\bar{E}^*(\bar{r},t)\bar{E}(\bar{r},t+\tau)dt. \quad (2.4.1)$$

For this equation to make sense, the ensemble average (indicated by the angled bracket) must be equal to the time average, which means that the process is assumed to be ergodic. This happens when the moving scatterers are present in the probed region [33]. Equation (2.4.1) gives a measure of the coherence loss between pairs of photons that emerge from the tissue with a time delay equal to τ. The normalized version of $G_1(\bar{r},\tau)$ is $g_1(\bar{r},\tau)$, and is given by:

$$g_1(\bar{r},\tau) = \frac{\langle \bar{E}^*(\bar{r},t)\bar{E}(\bar{r},t+\tau)\rangle}{\langle \bar{E}^*(\bar{r},t)\bar{E}(\bar{r},t)\rangle}. \tag{2.4.2}$$

Following the same reasoning, one can define the intensity correlation function:

$$G_2(\bar{r},\tau) = \langle \bar{I}^*(\bar{r},t)\bar{I}(\bar{r},t+\tau)\rangle = \lim_{T\to\infty}\frac{1}{T}\int_{-T/2}^{T/2}\bar{I}^*(\bar{r},t)\bar{I}(\bar{r},t+\tau)dt. \tag{2.4.3}$$

Also, its normalized version:

$$g_2(\bar{r},\tau) = \frac{\langle \bar{I}^*(\bar{r},t)\bar{I}(\bar{r},t+\tau)\rangle}{\langle \bar{I}^*(\bar{r},t)\bar{I}(\bar{r},t)\rangle}. \tag{2.4.4}$$

Both autocorrelation functions can be related to each other by the Siegert relation [34]:

$$g_2(\tau) = 1 + \beta|g_1(\tau)|^2. \tag{2.4.5}$$

The Siegert relation is derived from the original relation between the electric field and its intensity: $I = \varepsilon_0 c|\bar{E}|^2$. The β parameter will depend on the amount of detected speckle grains. Ideally, it will be equal to 1, but when unpolarized light is used and ideal optics are assumed, β will be equal to 0.5 [35].

In practice g_2 is the function that is usually measured experimentally. Now, by definition, $g_1(0) = 1$, which then gives the possibility of calculating the β parameter by doing: $g_2(0) = 1 + \beta$.

It is important to mention that, after a certain time, τ, coherence is lost, which will then lead to a decay in the curves of both g_1 and g_2.

2.5 Brownian Motion

DCS's results depend highly on the movement of the scatterers because g_1 depends on said movement [36]. Inside a biological tissue, red blood cells (RBCs) are the scatterer particles in the NIR. The average motion of RBCs in microvasculature can be modeled by Brownian

Motion. Whenever a particle is sufficiently small (around the order of a few microns), it will be able to interact with the molecules of the medium in which it is found, by colliding with them. This will provoke a random movement of the particle, which is the one called Brownian Motion. The same assumption was exploited in case of fruits.

One of the main parameters that describes this kind of movement is the diffusion coefficient, which is a parameter that defines how a particle will move inside a medium as time goes by. This coefficient is defined as [37]:

$$D_b = \frac{k_B T}{6\pi\eta r}. \tag{2.5.1}$$

In this equation, *T* is the absolute temperature, k_B is Boltzmann's constant, *r* is the radius of the particle, and η is the viscosity coefficient of the medium.

Another important parameter that needs to be considered is the mean square displacement, $\langle \Delta r^2(\tau) \rangle$. It represents a measure of the deviation that an ensemble of particles has with respect to a reference position during a time interval τ [38]. In case of Brownian motion, the following is true [1, 39]:

$$\langle \Delta r^2(\tau) \rangle = 6 D_b \tau. \tag{2.5.2}$$

Starting from this, and making the same approximations as the ones done to obtain the PDE from the RTE, the expression for g_1 can be rewritten as:

$$g_1(\tau) = \int_0^\infty P(s) e^{-i\omega t} e^{-\frac{1}{3}\langle \Delta r^2(\tau) \rangle k_0^2 s \mu_s'} ds. \tag{2.5.3}$$

Where *P(s)* is the normalized distribution of the photon path and *s* is the photon's path length. The wave vector of the incident field is given by k_0, while its frequency is ω [40]. Equation (2.5.3) shows that g_1 depends on the movement of the scatterers through their mean square displacement [40].

2.5.1 Diffusion of the Temporal Correlation Function

Starting from the fact that the electric field autocorrelation function characterizes temporal fluctuations of said field inside a medium, it can be demonstrated that modeling said function as having a random walk behavior, like the photons in the sample, is possible [1]. It is because of this reason that a diffusion equation can be written for $G_1(\bar{r}, \tau)$, by taking into account two important hypotheses [33]:

- Scatterers must be randomly oriented, and their dynamics isotropic, as in Brownian motion.
- The correlation time, τ, must be shorter than the time that a scatterer needs to travel a distance equal to a wavelength of the light being used.

Building from the above-mentioned information, a new diffusion equation, known as the correlation diffusion equation (CDE), can be derived:

$$\left[D\nabla^2 - v\mu_a(\bar{r}) - \frac{\alpha}{3}\mu_s' k_0^2 \langle \Delta r^2(\tau) \rangle\right] G_1(\bar{r}, \tau) = -vS(\bar{r}). \quad (2.5.4)$$

Here, D is the diffusion coefficient, α is the fraction of scattering events which occur from moving particles, $S(\bar{r})$ represents the source, and the square bracket encompasses the gradient of the correlation's flux together with the loss of correlation that happens due to the absorption and the scatterer's motion [1].

2.5.2 Semi-Infinite Homogeneous Media

In order to solve the CDE, the same approach as the one discussed in 2.3 to solve the PDE. This means that that a semi-infinite homogeneous media is assumed. In this case, though, a continuous wave (CW) source must be utilized.

One of the boundary conditions that is mentioned in 2.3 is the Extrapolated-zero Boundary Condition (EBC). This condition considers the presence of a fictitious negative source outside of the medium (Figure 2.4).

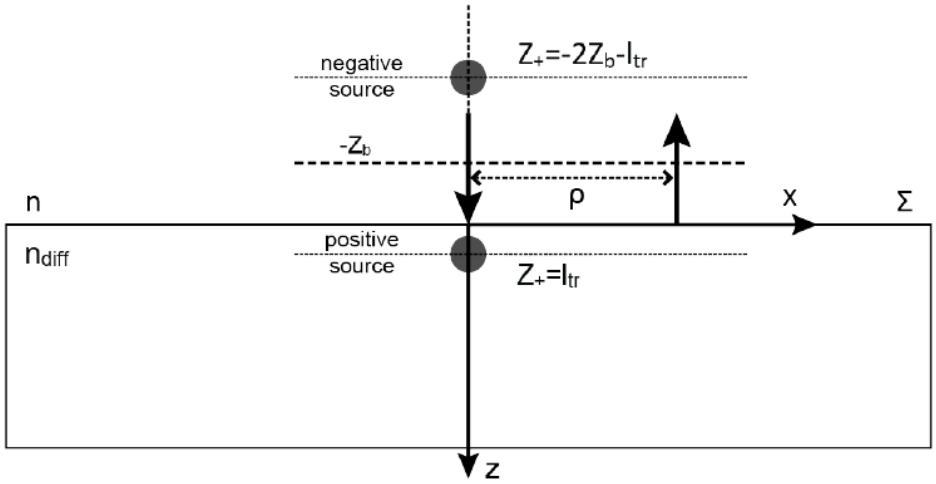

Figure 2.4 – Schematic of the EBC in a semi-infinite geometry. An infinite surface, Σ, separates a diffusive medium with a refraction index n_{diff}, from a non-diffusive medium with a refraction index n. The real source is approximated by an isotropic one, located at a depth of $z_+ = l_{tr}$. A negative source located at $z_- = -2z_b - l_{tr} = -4AD - l_{tr}$ is considered. The dashed line located at $-z_b$ represents the extrapolated zero boundary surface. The dark arrows represent both the injection and detection points, separated from each other by a distance ρ.

By summing the contributions of both sources present in the EBC, one can find the solution for the CDE:

$$G_1(\bar{r},\tau) = \frac{v}{4\pi D}\left[\frac{e^{-K(\tau)r_+}}{r_+} - \frac{e^{-K(\tau)r_-}}{r_-}\right]. \tag{2.5.4}$$

In the past expression, $K(\tau) = \sqrt{\frac{v}{D}[\mu_a + \alpha\mu_s' k_0^2\langle\Delta r^2(\tau)\rangle/3]}$, and also $r_+ = \sqrt{(z-l_{tr})^2+\rho^2}$ defines the distance between the positive source and the detection point, and $r_- = \sqrt{(z+2z_b+l_{tr})^2+\rho^2}$ is the distance between the detection point and the negative source [10, 11].

2.6 Autocorrelation Diffusion Equation with Static Background

The autocorrelation function $G_1(\bar{r},\tau)$ that has been discussed in the past sections has been built assuming that the scatterers are moving, but it does not take into account the characteristics of the background against which they are moving. In this section of the thesis, a new expression for $G_1(\bar{r},\tau)$ that takes a static background against the moving scatterers will be discussed. All the following information and discussions are based on the work done in [41], unless stated otherwise.

Beginning from the correlation transport equation (CTE), instead of the CDE discussed before, one considers the moving scatterers plus the static background instead of only the first ones to arrive to:

$$G_1(\rho,\tau) = -\frac{1}{4\pi}\left(\frac{z_{3,0}}{(\rho^2+z_{3,0}^2)^{\frac{3}{2}}}\left\{1+\left[\frac{\mu_A(\rho^2+z_{3,0}^2)}{D_c}\right]^{\frac{1}{2}}\right\}\exp\left\{-\left[\frac{\mu_A(\rho^2+z_{3,0}^2)}{D_c}\right]^{\frac{1}{2}}\right\}-\right.$$
$$\left.\frac{z_{4,0}}{(\rho^2+z_{4,0}^2)^{\frac{3}{2}}}\left\{1+\left[\frac{\mu_A(\rho^2+z_{4,0}^2)}{D_c}\right]^{\frac{1}{2}}\right\}exp\left\{-\left[\frac{\mu_A(\rho^2+z_{4,0}^2)}{D_c}\right]^{\frac{1}{2}}\right\}\right). \quad (2.6.1)$$

Many variables must be defined in equation (2.6.1):

- $z_{3,0} = -z_0$, where z_0 is given by $z_0 = (\mu_a + (1-g)\mu_s)^{-1}$, and g is the mean cosine between the directions of the photon before and after the interaction with the scatterer.
- $z_{4,0} = 2z_e + z_0$, where $z_e = 2AD_c$.
- $D_c = \frac{1}{3\{\mu_s[1-F_1(\tau)]+\mu_a\}}$.
- $\mu_A = \mu_s[1-F_0(\tau)] + \mu_a$.
- The coefficient A is a numerical value given in [28].

The terms $F_0(\tau)$ and $F_1(\tau)$ have more complicated expressions, mainly:

$$F_0(\tau) = \frac{P_m}{2}\left\{\sqrt{\frac{a\pi}{2g^3}}(g^2-1)\left[\operatorname{erf}\left(\sqrt{\frac{a}{2g}}(g-1)\right)+\operatorname{erf}\left(\sqrt{\frac{a}{2g}}(g+1)\right)\right]\exp\left(\frac{a(g-1)^2}{2g}\right)+\left(1-\frac{1}{g}\right)\exp(-2a)+1+\frac{1}{g}\right\}+(1-P_m). \quad (2.6.2)$$

And:

$$F_1(\tau) = \frac{P_m}{4}\left\{\sqrt{\frac{\pi}{2g^5a}}(g^4a + g^3 - a - g)\left[\mathrm{erf}\left(\sqrt{\frac{a}{2g}}(g-1)\right) + \mathrm{erf}\left(\sqrt{\frac{a}{2g}}\,(g+1)\right)\right]\exp\left(\frac{a(g-1)^2}{2g}\right) - \left(1 - g - \frac{1}{g} + \frac{1}{g^2}\right)\exp(-2a) + 1 + g + \frac{1}{g} + \frac{1}{g^2}\right\} + \; (1 - P_m)g. \tag{2.6.3}$$

Finally, P_m is the probability that a scatterer is moving and $a = \frac{1}{3}\left(\frac{2\pi n}{\lambda}\right)^2 \langle \Delta r^2(\tau)\rangle$.

Recalling equation (2.5.2), $\langle \Delta r^2(\tau)\rangle = \; 6D_b\tau$ for the case of Brownian motion.

Equation (2.6.1) can be normalized exactly as equation (2.4.1) and a new expression for g_2 can be obtained through the Siegert relation in the same way as before.

This new model will be utilized along with the classical one to analyze some of the results obtained in the experimental part of this thesis, presented in the following chapters. From now on, the models presented in this chapter will be referred to as “classical model” and “new model” for the semi-infinite homogenous model and the static-background model, respectively.

Chapter 3
System Architecture

This chapter focuses on explaining the schematics of the hybrid TRS-DCS device. Both the TRS and DCS parts of the system will be discussed here, focusing on the DCS' light injection system, detection components, and a brief explanation of the correlation algorithm that is used by the system to retrieve data. The final section of this chapter will explain briefly the materials used to work with the device, mainly epoxy and silicon phantoms, and different types of fruit.

3.1 DCS Device

The schematic build-up of the DCS module of the hybrid-device can be seen in Figure 3.1.

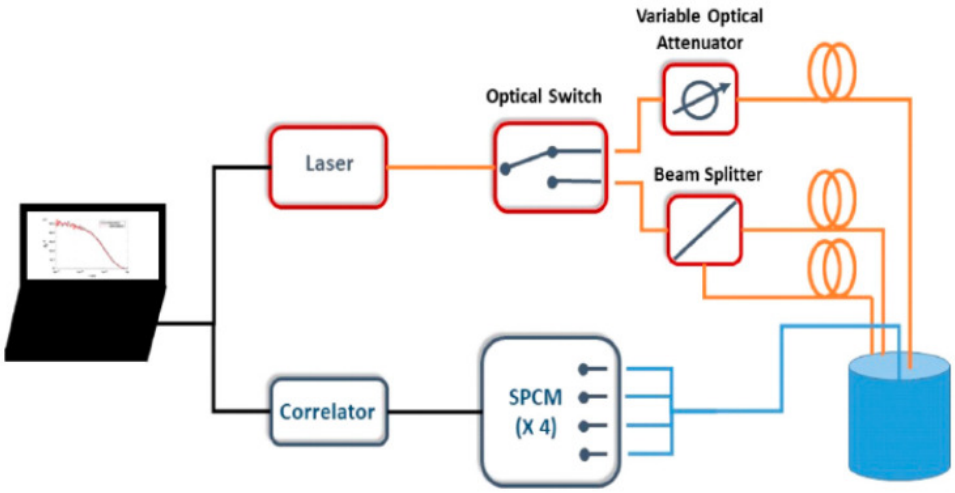

Figure 3.1 –Schematic representation of the DCS module of the hybrid-device [42].

The actual device can be seen in Figure 3.2.

Figure 3.2 – Hybrid DCS and TRS device during measurements on the forearm [42].

The device's mount that can be observed in Figure 3.2 is a 19" 4U module measuring $45 \times 40 \times 16$ (cm). Inside the mount, the DCS part is arranged in two different levels, as it can be observed in Figure 3.3.

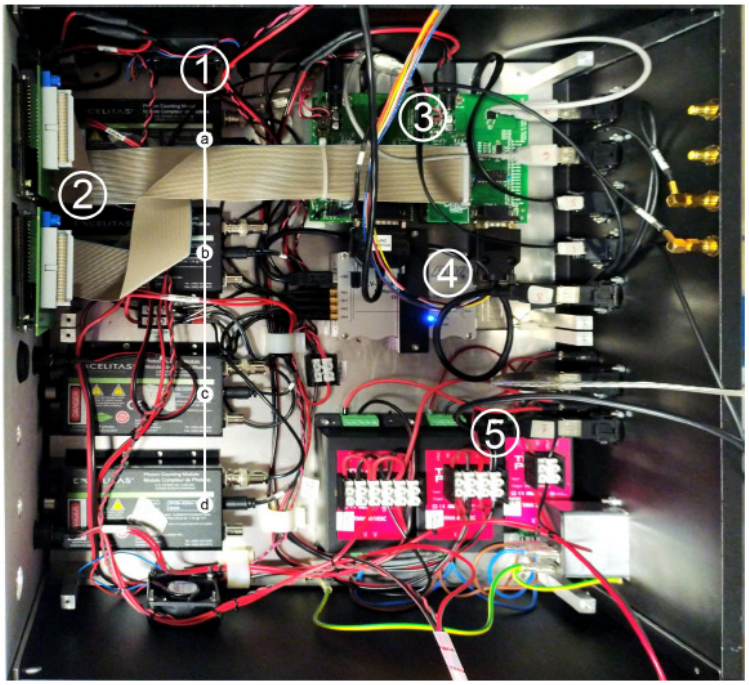

(a)

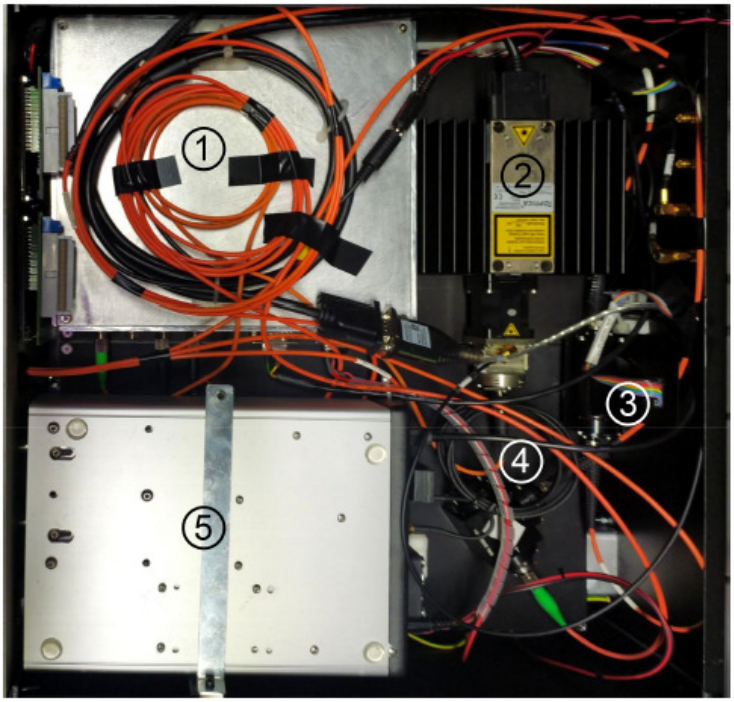

(b)

Figure 3.3 – Internal structure of the DCS device [42].

Figure 3.3 (a) depicts the bottom layer, which includes:

1. Four Single-Photon Avalanche Diodes (SPAD, SPCM-AQRH-3XSPAD, Excelitas Technologies Corp. Miamisbrug, OH, USA), which are used to detect backscattered light.
2. LCD screens to control the optical switch and the attenuator are shown.
3. Two microcontrollers (dsPIC30F6016, Microchip Technology Inc., Chandler, AZ, USA), used for the optical switch and the attenuator, synchronizing them with the correlator.
4. Digital correlator (ALV 70004USB/FAST, ALV-GmbH, Germany) that retrieves the intensity autocorrelation function.
5. Transformers for converting the input voltage (220 V) to 12 V (which supply the lasers and the fans), and 15 V (which supply the TRS module) to 5 V (which supply all the other components).

Figure 3.3 (b) shows the upper layer of the setup, which has:

1. Switch (mol $2 \times (2 \times 2)$, LEONI Fiber Optics GmbH, Jena, Germany) that alternatively sends the optical signal to two branches.
2. A highly coherent continuous-wave diode laser (iBeam Smart, TOP-TICA Photonics AG, Munich, Germany).
3. Optical attenuator (DD-200-55-785-400/430, OZ Optics LTD., Ottawa, Canada).
4. Beam splitter (FOBS-12P-111-400/430, OZ, Optics LTD., Ottawa, Canada), that divides the optical signal into two different branches.
6. TRS device, discussed with more detail in section 3.3, which is synchronized to the DCS module through logic signals.
5.

3.1.1 Light Injection and Detection

A long coherence length laser is used as the system light source because the DCS technique is based on measuring the coherence loss of the incident light [39]. The injection section consists of the highly coherent continuous-wave diode laser previously mentioned. It operates at 784 nm wavelength and its coherent length is greater than 8 m. The maximum power emitted by the laser is 120 mW, and can be controlled through a software installed in a PC. This laser's light is coupled to a step-index glass optical fiber (100/125 μm core/cladding, OZ Optics Ltd., Ottawa, Canada), which is then directed to an optical switch. This switch directs the light into both an optical attenuator and a beam splitter, alternating

between them and synchronized with the acquisition by a microcontroller. A fan is installed next to the laser to dissipates the heat, preventing the device from overheating.

On the other side, for light detection, a bundle of four single-mode optical fibers (5 μm core, numerical aperture = 0.13) directs the backscattered light that comes from the tissue into the four single-photon avalanche diodes. These previously mentioned SPAD are a type of photodetectors that can detect signals with low intensity, even single photon counts. They have a high temporal resolution that allow to reveal the arrival of the photon with an accuracy of tens of picoseconds. The detectors' electrical output is then converted into a TTL pulse for each detected photon [1], which are then directed into an autocorrelator board.

3.1.2 Injection Path

In Figure 3.1, one can see that the laser is directly connected to an optical switch, that divides the incident light and directs it through two different paths. The first one goes to the attenuator, which is then connected to an optical fiber (400/430 μm core/cladding, OZ Optics Ltd., Ottawa, Canada) that is mounted on the optical probe 1 cm away from the detection point. The second path goes to the beam splitter, which further divides the light into two lines again.

3.2 System Correlator and the Multiple Tau Correlation Function

A 4-channel digital correlator receives the signal detected by the SPAD. To compute a high precision correlation function estimator over a wide enough range of lag times, using only a small number of correlation channel estimators, the correlator uses a technique called Multiple Tau Correlation. To describe it, a brief introduction to the basic concepts behind correlation function measurements is presented in this section. A more detailed discussion and further information can be consulted in [43, 44].

3.2.1 Linear Correlator

A digital correlator with a channel configuration that has linear spacing is called a linear correlator. It can do four main fundamental operations, which are [45]:

- Counting photoelectron pulses over sampling time intervals with a width δ.
- Delaying the samples by an integer multiple of δ. This is called the lag time: $\tau_j = k\delta$.

- Multiplying the delayed and direct data samples.
- Sum these products.

Besides the sampling time, another main parameter of the correlation system is the dynamic range. It is determined by $\tau_j = k\delta$, where each value of k is corresponding to a particular correlation channel and is called lag. When the value of the dynamic range reaches 10^{12}, the correlation functions will require a high amount of correlation channels, but increasing their amount without any restrain is impossible in actual hardware design. This leads to a time resolution limit and decrease that affects the obtained results. Therefore, a linear correlation approach features two main limitations:

- It is difficult to cover a large lag time range.
- There are constant and fixed, sampling time intervals.

The problem has tried to be tackled with the introduction of exponential sampling time correlators, but results have not been satisfactory. In fact, decaying correlation functions will be affected by the lacking increase of sampling times and from the fact that most of the information of the correlation function is not even computed.

On the other hand, the second limitation stems from the nature of the process. A photon correlation experiment can be considered to have multiple process decaying functions. These processes can further be divided into sub-processes that have an average fluctuation frequency, f_p. Therefore, the correlation functions obtained from here will have some particular properties:

- For lag times much shorter than $\frac{1}{f_p}$, the correlation function will be almost constant.
- For lag times much longer than $\frac{1}{f_p}$, a larger sampling time will increase the statistical accuracy of the baseline without impacting the correlation function itself, because for this process it has decayed to an almost zero value.
- In cases in between the first two, when the sampling time is close to $\frac{1}{f_p}$ is when the changes in the correlation function are most observable. In particular, when the sampling time is a little shorter than $\frac{1}{f_p}$, it will process with the best statistical accuracy without distorting the correlation function.

Due to these limitations, a linear correlator cannot address strong multi-process situations, at least efficiently, no matter the number of channels utilized. As $\frac{1}{f_p}$ becomes larger, the processes suffer from a sampling time that is too short, while when it becomes smaller, then the process cannot be sampled by a long sampling time without them having to deal with high temporal integration effects. The solution to these limitations is found in a multiple tau correlator, discussed in the following section.

3.2.2 Multiple Tau Correlation Technique

This technique overcomes the limitations of the linear correlator by using multiple sampling times, but instead of increasing δ from channel to channel, a number of correlation channels that is equal or greater than eight is selected, form one block with a common δ, which is then doubled from one block to another [43]. This can be seen with more detail in Figure 3.4.

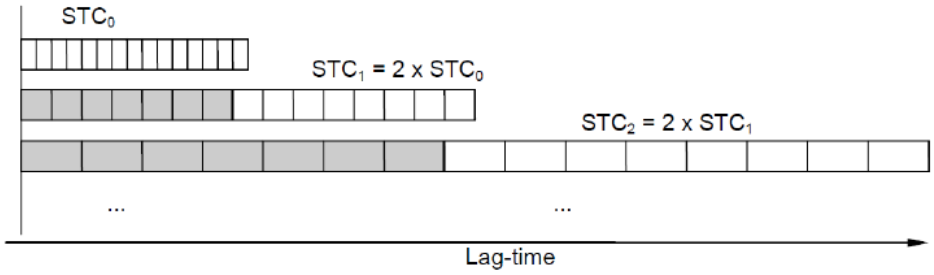

Figure 3.4 – Multiple tau correlation technique. Square cells represent the duration of the sampling time, while the gray cells represent the redundant information coming from the first channels [44].

The redundant information obtained from the first channels (gray blocks in Figure 3.4) can be removed by selecting the correlation channels that cover a lag time regime that has not been covered previously.

The main advantage of the logarithmic delay spacing is that it allows to cover large lag time ranges with a small number of channels without information loss, and requires that the width of the sampling interval, δ, increases in proportion to the lag time. In this thesis, the device utilized is an ALV correlator with a minimum integration time of 1 second, a 3 ns delay time, and 200 channels.

3.3 TRS Device

The TRS part of the system is not the focus of this work, but it will be briefly presented here for the sake of completeness.

This device allows to quantify the wavelength-dependent optical absorption and scattering coefficients of the probed tissue. These values can be then utilized along with the DCS device to obtain information on the diffusion coefficient of the analyzed tissue. Work to detail the properties of the TRS module have been done before and can be consulted in [8]. The schematic representation can be consulted in Figure 3.5.

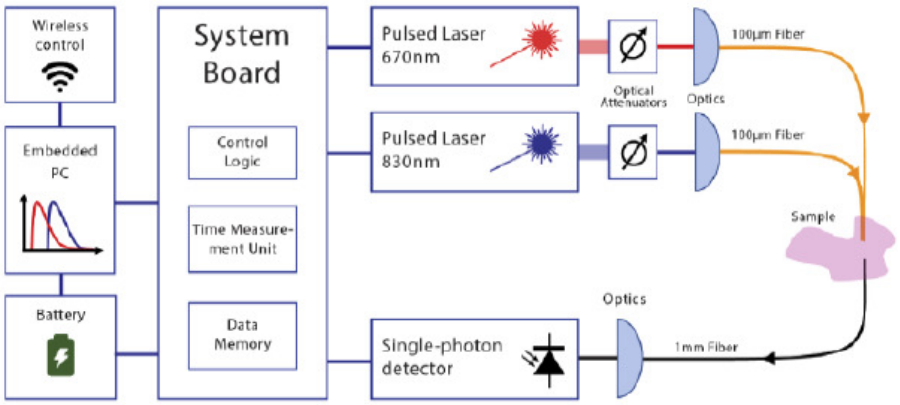

Figure 3.5 – TRS device schematic diagram [8].

The light sources are two pulsed diode lasers that emit light at 670 nm (average output power of 4 mW) and at 830 nm (average output power of 3.5 mW). Each wavelength is coupled to a 1 mm graded-index plastic optical fiber (numerical aperture of 0.29, FMC, Italy) after passing through an optical attenuator. One injection point is made by putting together in a bundle the fibers from both lasers. The beams are injected and collected through a flexible probe that has a prism allocated inside in order to reflect the light 90º. Different probes can be 3-D printed in order to have access to different inter-fiber distances (the distance between the source and the detector's fiber). The backscattered light coming from the sample is collected by another graded-index Plastic Optical Fiber (POF) that has a core diameter of 0.9 mm. The photons coming from the sample are then detected by a silicon photomultiplier (SiPM) that has an active area of 1.7 mm^2, and is coupled to the detection fiber.

Afterwards, a time-to-digital converter reconstructs the optical waveforms by measuring the arrival times of the observed photons. The system is controlled by an embedded PC which employs custom software designed for this task.

In order to analyze the collected data, the acquired data were fitted with the curve obtained from the analytical solution for the classical model for photon diffusion and convolved with the instrument response function (IRF). This yields both the absorption coefficient and the reduced scattering coefficient as a result, which can then further be utilized to analyze the data with the DCS device.

3.4 Sample Materials

This work utilized two main materials to study the response of the DCS device: phantoms and fruits. The phantoms were made of different materials, such as epoxy and silicon. One liquid phantom was also utilized. Fruit, on the other hand, were varied. From apples and oranges, to tomatoes and aubergines, many different types were utilized.

3.4.1 Phantoms

Solid phantoms were mainly utilized because they serve as a reference standard. They are fabricated in such a way that their optical properties (mainly, the absorption and scattering coefficients) are known and constant, but not their dynamical properties (the diffusion coefficient), which is what it is tried to be measured with this experiment. The epoxy and silicon phantoms were fabricated in the laboratory, but its fabrication is not part of the objectives of this work. For the liquid phantom, one provided by HemoPhotonics was used, because it is a non-biodegradable, water-based solution of polydisperse microparticles that is stable over time and has well known optical and dynamical properties, as opposed to the solid phantoms, as previously mentioned.

The phantoms were analyzed with both models explained in chapter 2 of this work, mainly in sections 2.4 and 2.6. In the next chapter, the result of these analysis and comparisons are presented and discussed.

3.4.2 Fruit

In our knowledge, fruit has not been analyzed before with a DCS device, so the objective here was to see how well the properties of different types of fruit can be characterized with it. Many different types were used:

- Aubergines
- Tomatoes
- Apples
- Lemons
- Limes
- Oranges
- Tangerines
- Kiwi

This has been done because different types of fruit can have very different characteristics from each other. Two approaches were taken for the fruit analysis: the first one was to group together different types of fruit and analyze them in order to see, first, how well the utilized models fit the results obtained from them, and second, to see how the results change between each type of fruit. For this, two groups of fruit were used: one that consisted of an aubergine,

lemon, lime, orange, tangerine, and a tomato, and another made up by the same fruits, with the exception of the tangerine and lime, which were replaced with a kiwi. This second group of fruit was also analyzed without their peels in order to see how (or if) the results changed.

The second approach involved analyzing various fruits of the same type. In this case, a group of apples and a group of tomatoes were both analyzed, and the results obtained for each individual fruit of a certain group were compared to the other analyzed fruits of the same type.

3.4.3 Probes

Probes are 3-D printed pieces that allow the user to mount the source and the detector's optical fibers at certain distances from each other. These probes are designed with the *AutoDesk Inventor* software before being printed. They must meet certain requirements:

- Ensure that the light captured in the detection fibers is coming only from the sample being analyzed, therefore preventing the passage of direct light from the source to the detector. This is due to the fact that direct light coming from the source will have a higher coherence degree than the diffuse light coming from the sample, which can greatly change the obtained results.
- The probes must be designed to hold the optical fibers firmly, without the need of external aids like adhesive, or glue.

In figure 3.6, two example of the probes used for this thesis can be observed. Here, the probes were printed with a flexible material (PoliFlexTM, Polymaker, Suzhou, China) that allows them to adapt to the surface of the sample being analyzed, and contains both the DCS and TRS optical fibers. These fibers are coupled to the tissue through a prism that redirects light 90^{o}, thus preventing the fibers from bending and staying parallel to the surface of the sample. The probes' material not only adapts to the sample's surface, but also adheres firmly to it, preventing movement during its utilization [42]. In this particular image, the first probe has interfiber distances of 1 and 2.5 cm, while the second probe has a fixed interfiber distance of 2 cm.

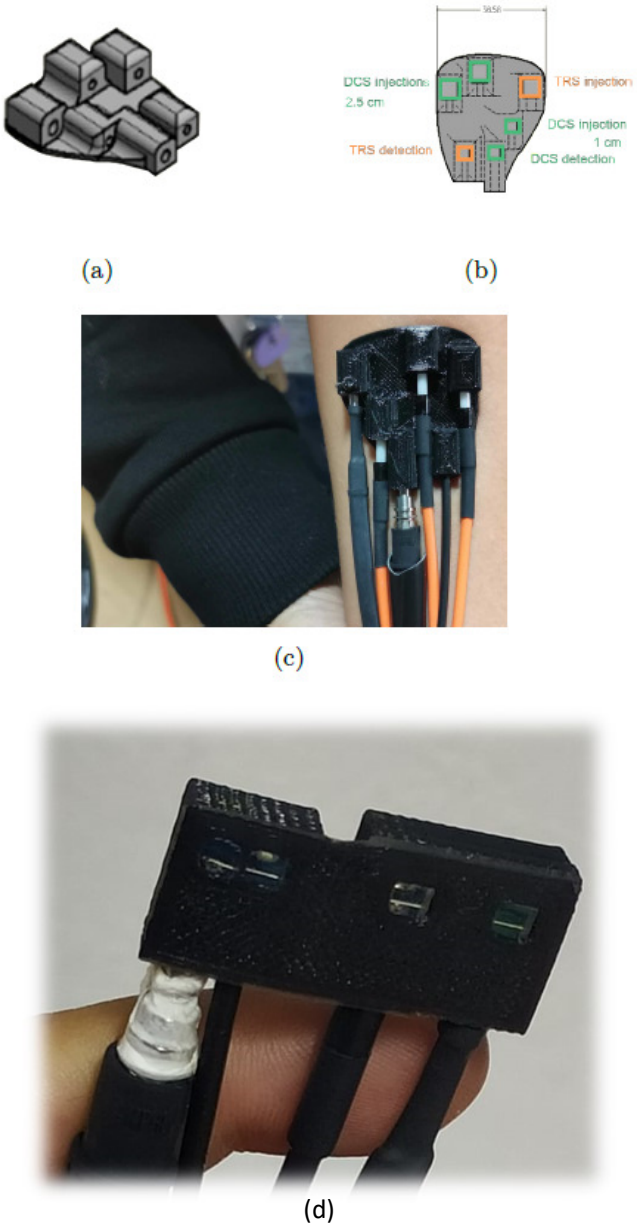

Figure 3.6 – (a) Lateral view of the 3-D probe. (b) Dimensions of the probe (cm), where the green boxes represent the DCS injection and detection points and the orange ones represent the same for the TRS part. (c) Probe utilized in an in vivo measurement [42]. (d) Probe with an interfiber distance of 2 cm used for the majority of the measurements done in this thesis.

Different interfiber distances were used to try to reduce superficial effects. The first group of fruit mentioned in the previous section was analyzed with a probe that had two different interfiber distances: 1 cm and 2.5 cm. This was done to check if there was any difference

between them due to the heterogeneity of the fruit. Then, the probe was changed to one which had a fixed interfiber distance of 2 cm. This new probe was utilized for the measurements in the apple and tomato groups, and also for the totality of the phantoms. Finally, for the last group of varied fruit, a probe with a fixed interfiber distance of 1.5 cm was used. This smaller distance was used also for the measurements that were performed without the peel of the fruits.

Chapter 4
Phantom Results

The results obtained for the phantoms mentioned in the previous chapter are presented in this chapter, along with its respective analysis.

Three types of phantoms were measured with the device: silicon, epoxy and a liquid phantom. A total of 300 measurements per phantom were taken with an acquisition time of 1 second. The chosen interfiber distance was of $\rho = 2$ cm and the assumed refractive index has that has been used is 1.33.

Three sets of phantoms were used for the silicon variety, with one, two, and three phantoms per set respectively. One set of three phantoms was analyzed for the epoxy kind, while the liquid phantom analyzed is the one provided by HemoPhotonics.

First, the absorption and scattering coefficients for each phantom were obtained through the TRS device. Once this was done, these values were introduced into a MATLAB code designed to obtain the electric field and intensity autocorrelation functions mentioned in chapter 2. A fit for these curves is also calculated using the previously commented theoretical models. Mainly, the classical model has been used to analyze every set of data for the phantoms, while the new model, which takes the static background into account, has been used in particular cases to compare the results. These cases will be explicitly stated when used.

The analysis with the MATLAB model has been run three different times. The first one was done analyzing each individual data file (one per measurement realized), thus obtaining results for every second of measurements. The second time, the code was modified to average the measured autocorrelation functions into groups of five and analyze the new results, thus obtaining information for every five seconds of measurements. Lastly, the same kind of analysis was performed, now for every ten seconds of measurements. This was done with the objective of seeing if the fitting curve improved through this approach.

Also, through this analysis, the MATLAB model calculates the values of both the diffusion coefficient, D_B, and β, used in the Siegert relation (equation 2.4.5).

4.1 Epoxy phantoms

Three different epoxy phantoms were analyzed. In the following, the autocorrelation functions obtained for one of them (for the sake of simplicity), along with their respective fits, are presented.

4.1.1 Phantom label: Epoxy_1

Examples of the fitting curves obtained for this phantom can be seen in Figure 4.1:

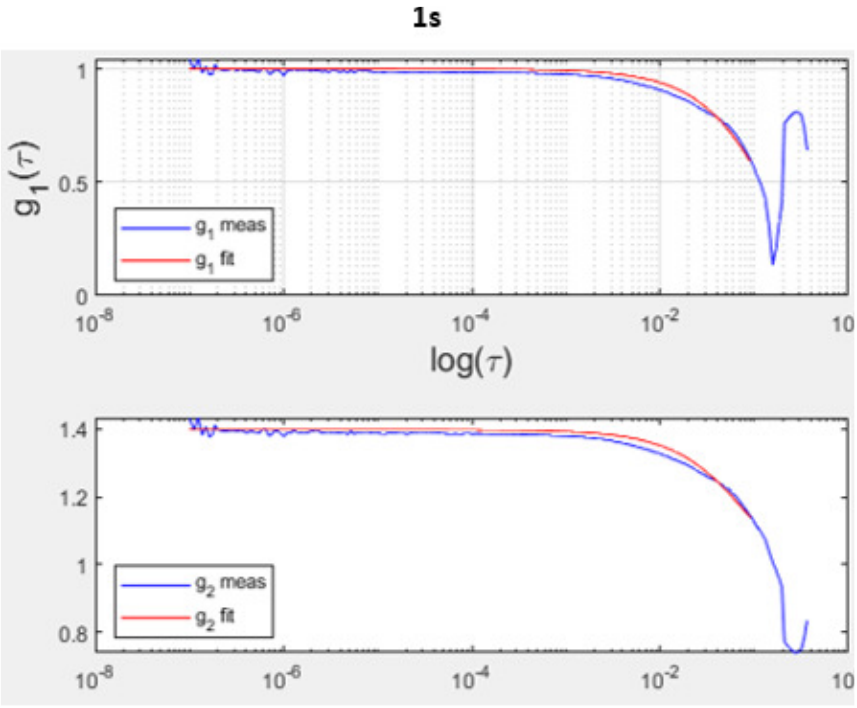

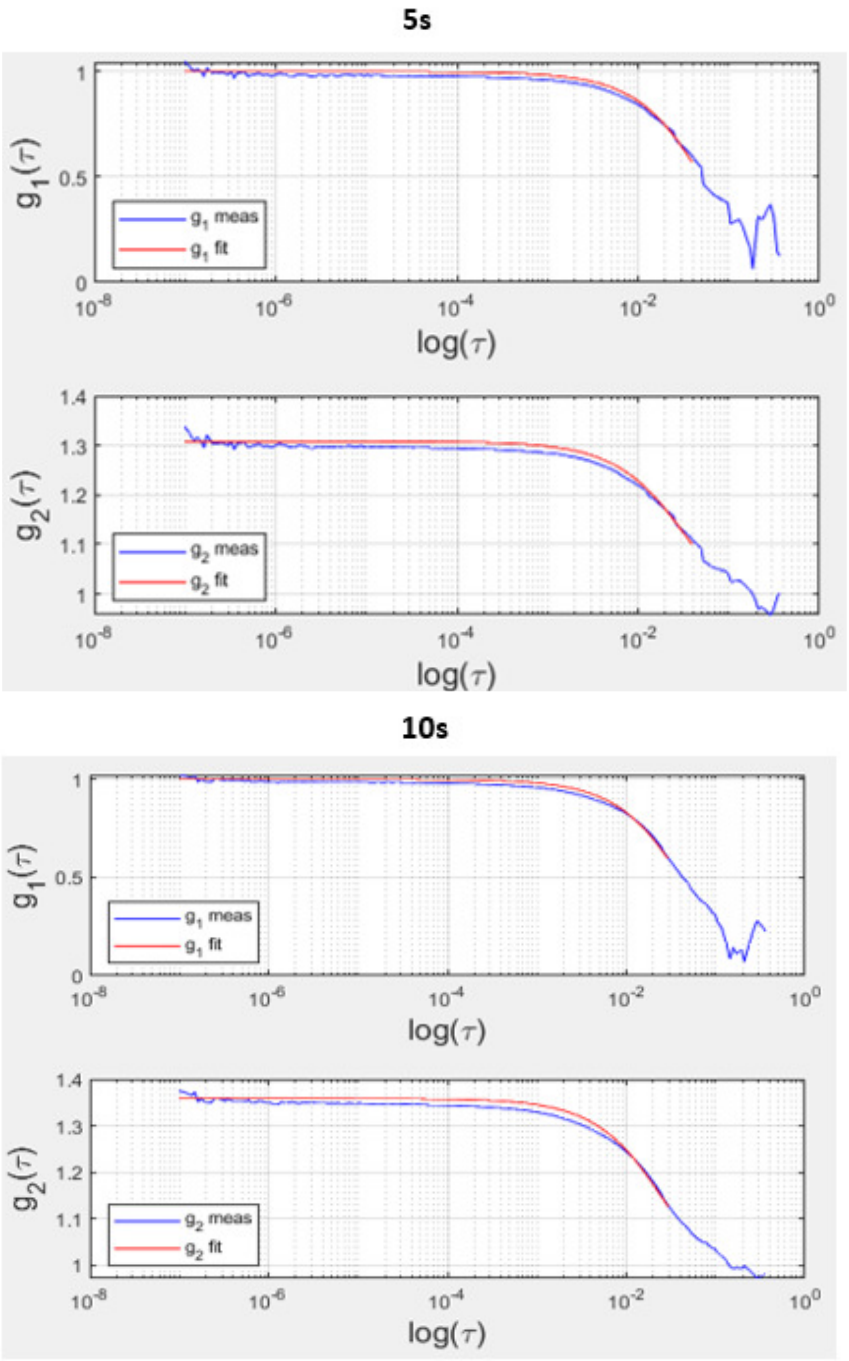

Figure 4.1 – Curves obtained, both g1 and g2 (blue) for an epoxy phantom with different acquisition times of 1 second (top), 5 seconds (middle) and 10 seconds (below). Their respective fits are shown in red.

It can be clearly seen that the fit is not perfect, though a small improvement can be noticed going from 1 second to higher acquisition times. Both the 5 and 10 second graphs seem to be a slight improvement compared to the 1 second graphs.

In terms of the diffusion coefficient, D_B, and β, the obtained results can be seen in figure 4.2.

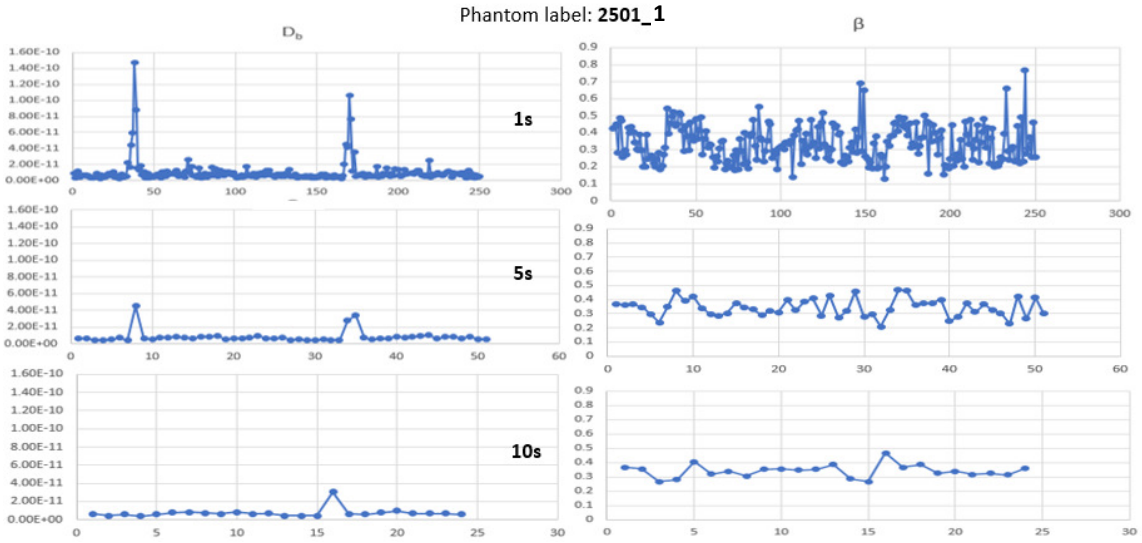

Figure 4.2 – Values obtained for D_B and β in different acquisition times of 1, 5, and 10 seconds for an epoxy phantom.

The values obtained have been filtered to discard certain useless values that were represented as "not a number" (NaN) during the analysis (this has been done also for every other case presented in this work). These results are expected to be close to constant, but it can be observed that they are not. The diffusion coefficient presents huge peaks in different areas that actually diminish as the acquisition time increases, while the value for β fluctuates a lot between files. As it will be seen, this is the case for the rest of the obtained results in this chapter.

In this particular case, the peaks observed for the diffusion coefficient are very high. Usually, as seen with other phantoms in the following sections, the value for the diffusion coefficient fluctuates in ranges that remain relatively constant for each particular phantom.

The average values obtained both for D_B and β, along with their standard deviations, are presented in the following table.

Table 4.1 – Average value and standard deviation of both D_B and β obtained for an epoxy phantom.

	Average D_B	Average β	St. Dev. Of D_B	St. Dev. Of β
1s	$9.34\text{x}10^{-12}$	0.3306	$1.378\text{x}10^{-11}$	0.1053
5s	$8.15\text{x}10^{-12}$	0.3339	$6.964\text{x}10^{-12}$	0.0674
10s	$8.06\text{x}10^{-12}$	0.3339	$6.279\text{x}10^{-12}$	0.0529

The values for the diffusion coefficient are not good, as it can be seen that its standard deviation is of the same order of magnitude (and bigger, in the case of one second) as the average value. This should be the opposite; one would expect it to be significantly lower. For the case of β, its values remain relatively constant for the different acquisition times, while the standard deviation decreases as the time increases.

By observing all of the obtained autocorrelation functions together, as pictured in Figure 4.3, one can see that the results are varying in a significant way from second to second. Even though individual curves cannot be distinguished in the figure, the fact that the area they are covering is so wide means that they are all over the place, instead of being as similar to each other as possible, as it should be expected. When taking into account the curves for every 10 seconds of acquisition time, (Figure 4.3, below), the situation improves slightly for g_1, where it can be seen that the decay, even though it is still varying considerably, begins to group itself in a smaller range than in the 1 second case (Figure 4.3, above). This is not the case for g2, where the variation of the curves can still be seen without any trend to group itself in a particular range.

Figure 4.3 confirm that the high standard deviation observed for these measurements is not strictly related to a failure of the model of analysis, but the measured autocorrelation curves strongly differ from each other.

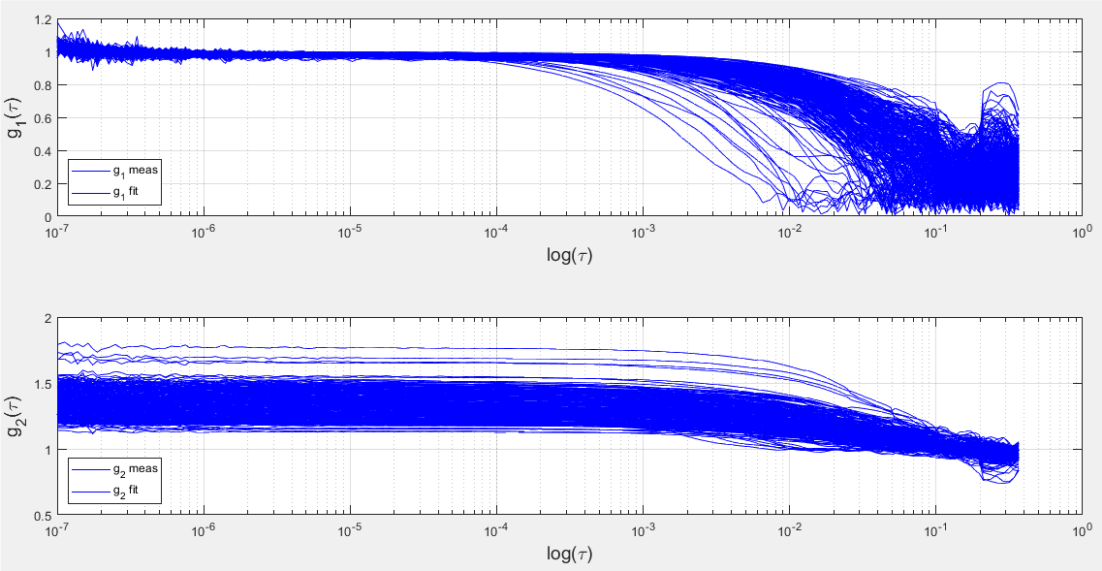

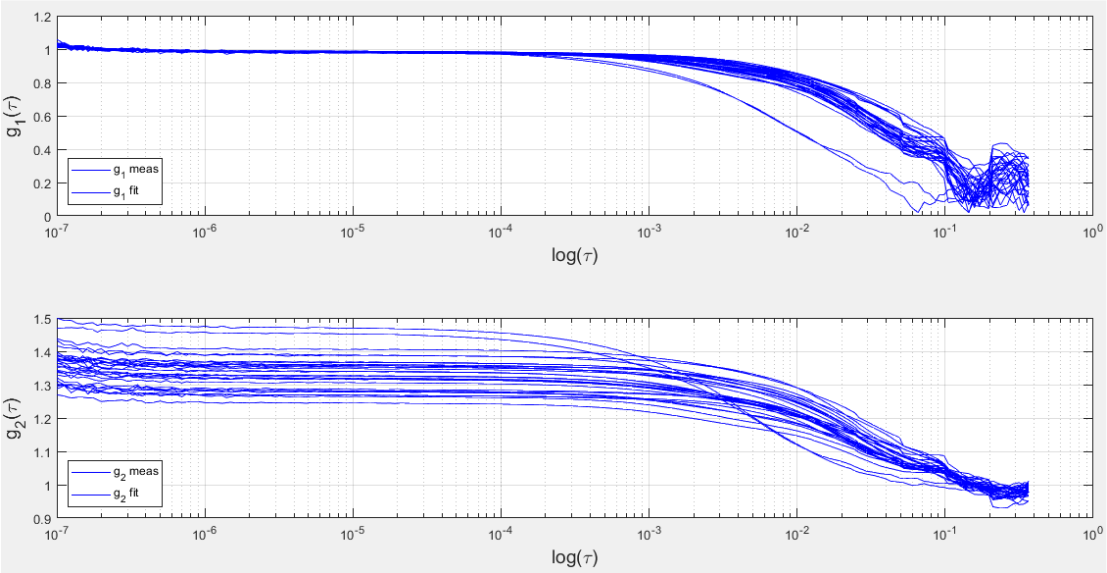

Figure 4.3 – All of the curves obtained for the epoxy phantom are presented here (1 second case above, 10 second case below). The g_1 curves begin relatively equal to each other while their decay varies a lot. For g_2, the curves have varied ranges in general, and not only in a particular area as g_1.

4.2 Silicon phantoms

Six different silicon phantoms were analyzed. The results obtained for one of them are shown in the following subsection as an example, as the results for all of the phantoms were similar to each other.

4.2.1 Phantom label: Sylgard_0802_1

Examples of the fitting curves obtained for this phantom are presented in Figure 4.4.

1s

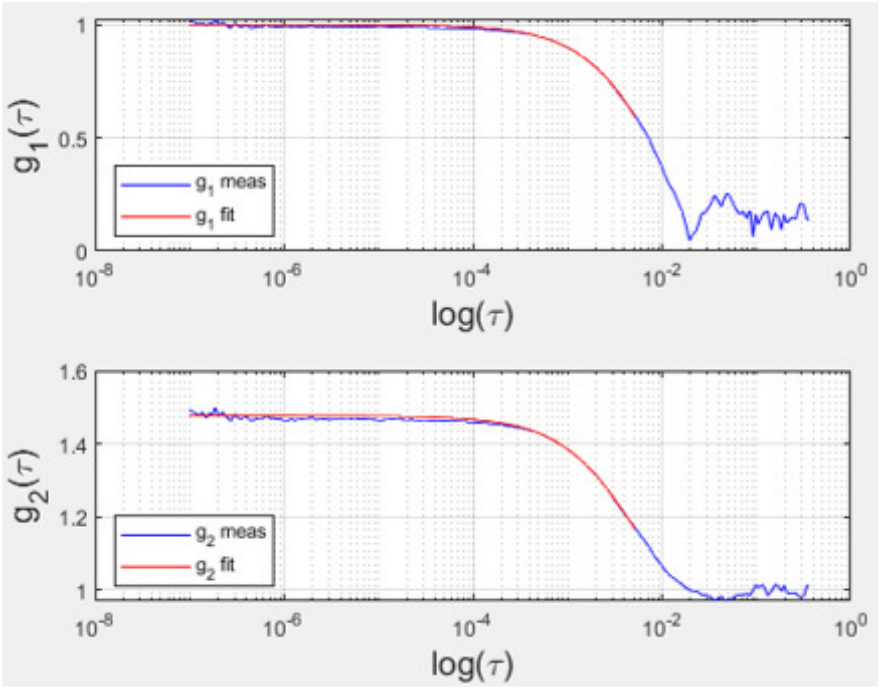
$g_1(\tau)$
g_1 meas
g_1 fit
log(τ)
$g_2(\tau)$
g_2 meas
g_2 fit
log(τ)

5s

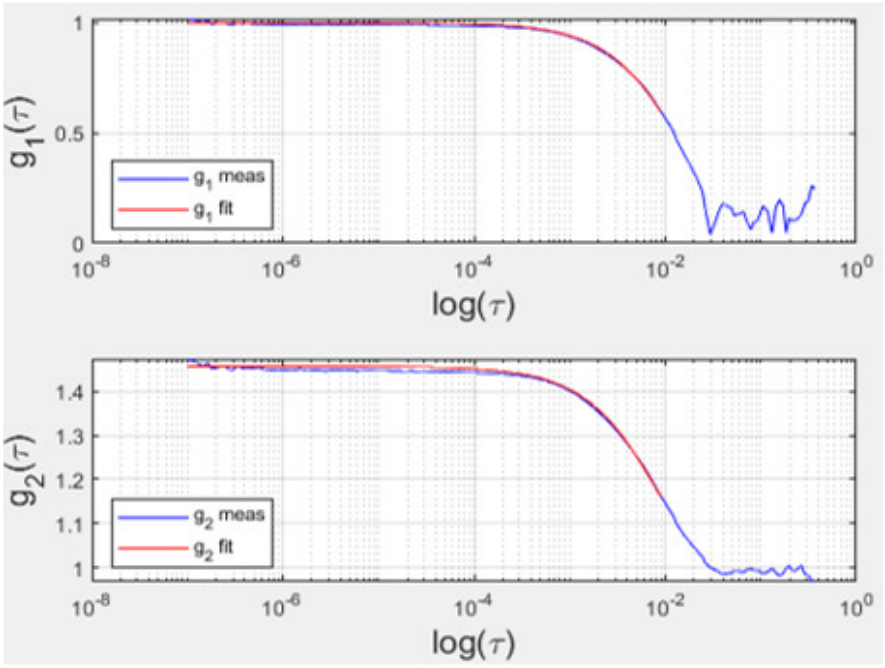
$g_1(\tau)$
g_1 meas
g_1 fit
log(τ)
$g_2(\tau)$
g_2 meas
g_2 fit
log(τ)

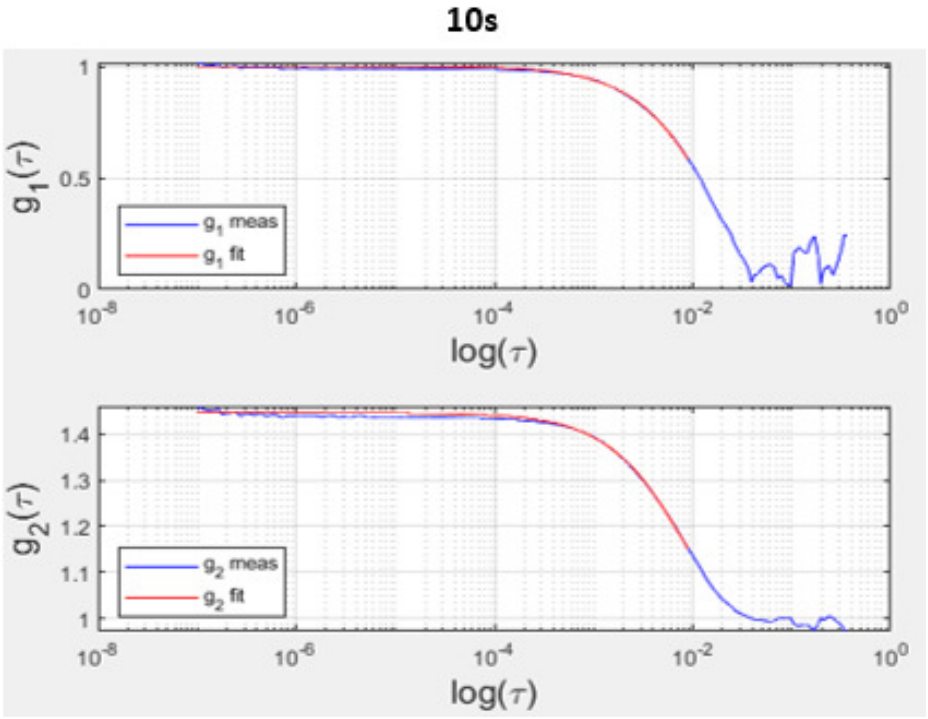

Figure 4.4 – Curves obtained, both g1 and g2 (blue) for a silicon phantom with different acquisition times of 1 second (top), 5 seconds (middle) and 10 seconds (below). Their respective fits are shown in red.

The fits in Figure 4.4 are much better than the ones for the epoxy phantom. For the three different acquisition times, the fit is almost perfect and adapts well to the obtained curves. This is what should be expected from the model that is being utilized to analyze the data.

Speaking of the diffusion coefficient, D_B, and β, the obtained results can be seen in figure 4.5.

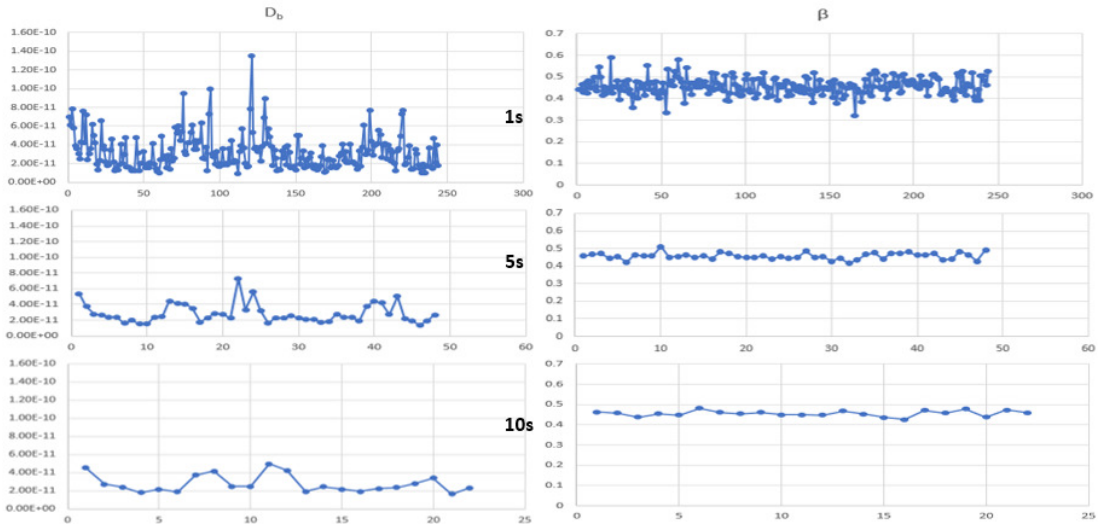

Figure 4.5 – Values obtained for D_B and β in different acquisition times of 1, 5, and 10 seconds for a silicon phantom.

The results shown in Figure 4.5 are an improvement compared to the epoxy phantom. This is mostly due to the fact that this case does not present peaks in the diffusion coefficient that are as prominent as the ones seen in Figure 4.2. Regardless of that comparison, the results are still far from ideal. The diffusion coefficient still shows fluctuations that are not negligible. Even though, again, these fluctuations do diminish as the acquisition time increases.

Table 4.2 – Average value and standard deviation of both D_B and β obtained for a silicon phantom.

	Average D_B	Average β	St. Dev. Of D_B	St. Dev. Of β
1s	$3.27\text{x}10^{-11}$	0.4570	$1.934\text{x}10^{-11}$	0.0395
5s	$2.93\text{x}10^{-11}$	0.4581	$1.251\text{x}10^{-11}$	0.0182
10s	$2.86\text{x}10^{-11}$	0.4578	$9.856\text{x}10^{-12}$	0.0133

The values obtained for the diffusion coefficient improve for the silicon phantom compared to the epoxy phantom, as the standard deviation is now smaller in every case than the average value, but it is still not as small as desired, being of the same order of magnitude in two out of the three evaluated cases. The situation with β is different, though, as the standard deviation is indeed considerably smaller than the average value, and also, as the acquisition time increases, the value of the average fluctuates less between each case. This is closer to the expected results in the phantom analysis.

Finally, Figure 4.6 shows the comparison between the curves obtained for acquisition times of 1 second (above) and 10 seconds (below). Like with the epoxy phantom, the curves can be seen to be covering a wide variety of ranges. This can be seen again in the decaying part of the g_1 curves, where the range of the decaying curves covers almost two orders of

magnitude in the x-axis. The range of the g2 curves, on the other side, seems to be more localized than with the epoxy phantom, and this difference can be noticed further when going from the 1 second acquisition time (Figure 4.6, above) to the 10 seconds one (Figure 4.6, below).

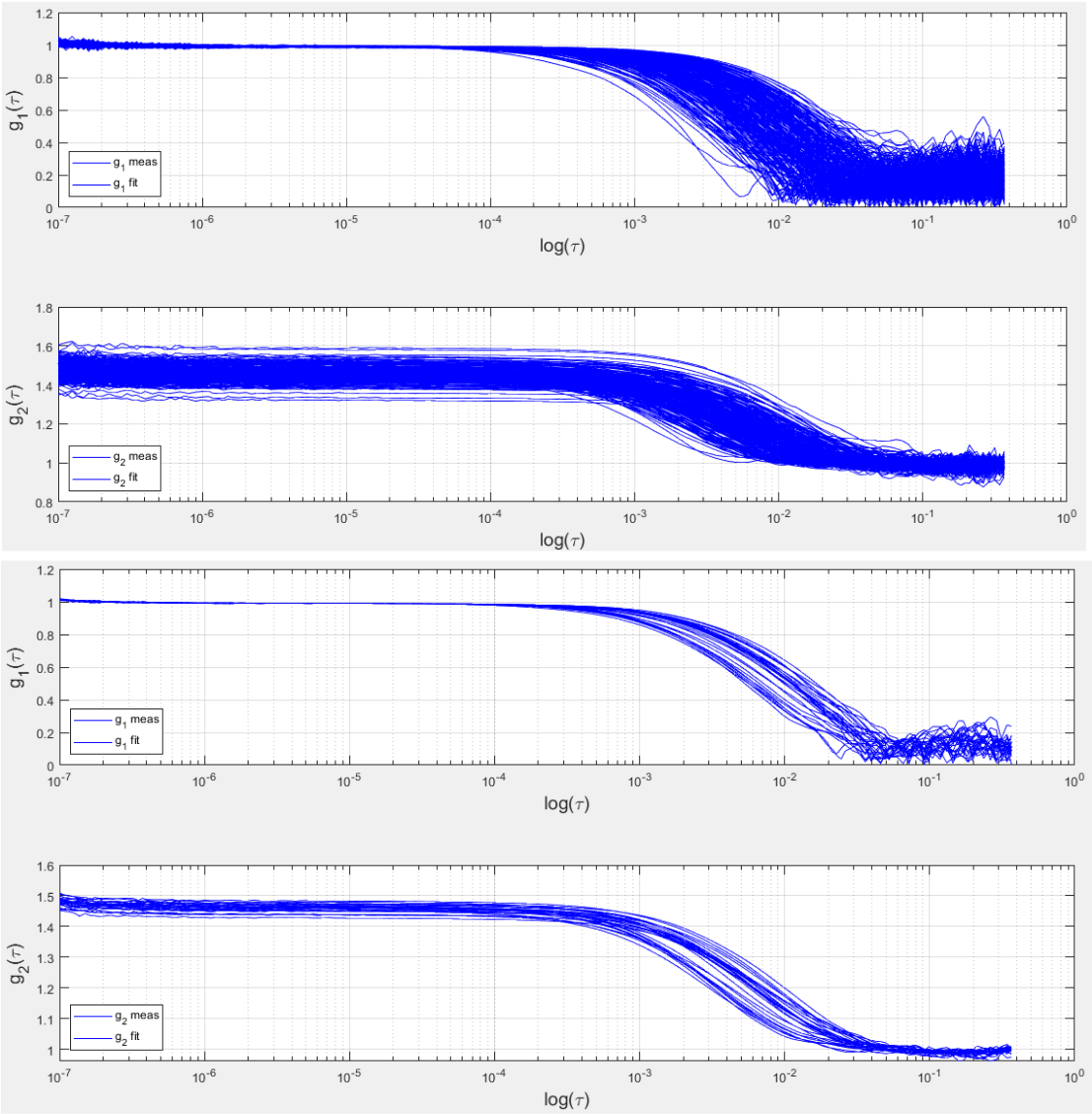

Figure 4.6 – All of the curves obtained for the silicon phantom are presented here (1 second case above, 10 second case below). The g_1 curves begin relatively equal to each other while their decay considerably varies. For g_2, the curves have varied ranges in general, but not as varied as in figure 4.3.

Overall, the behavior of the silicon phantom seems to be more reliable than the epoxy one.

4.3 Liquid phantom

The only liquid phantom that was analyzed during this work has already been introduced at the beginning of the chapter. It has also been studied before [11]. The results obtained with this particular study are shown in the following figures.

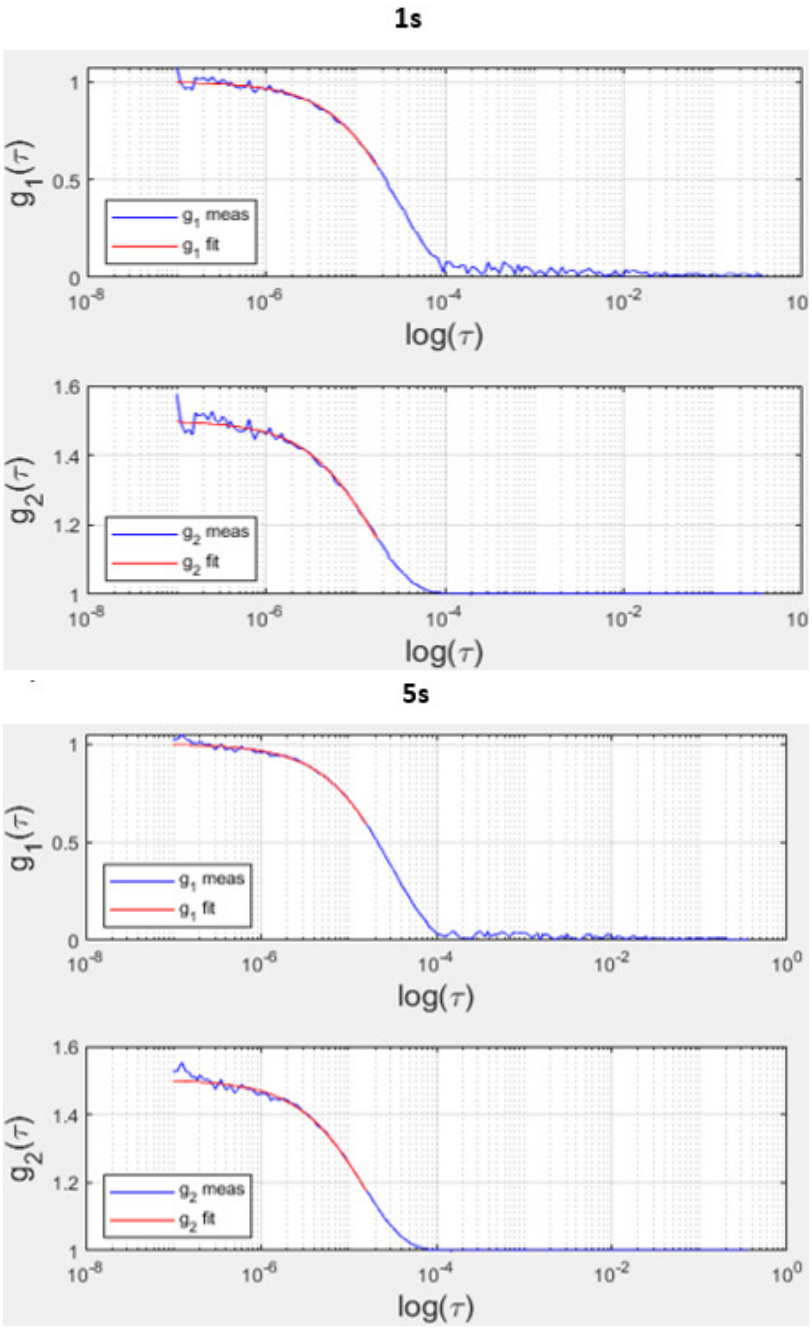

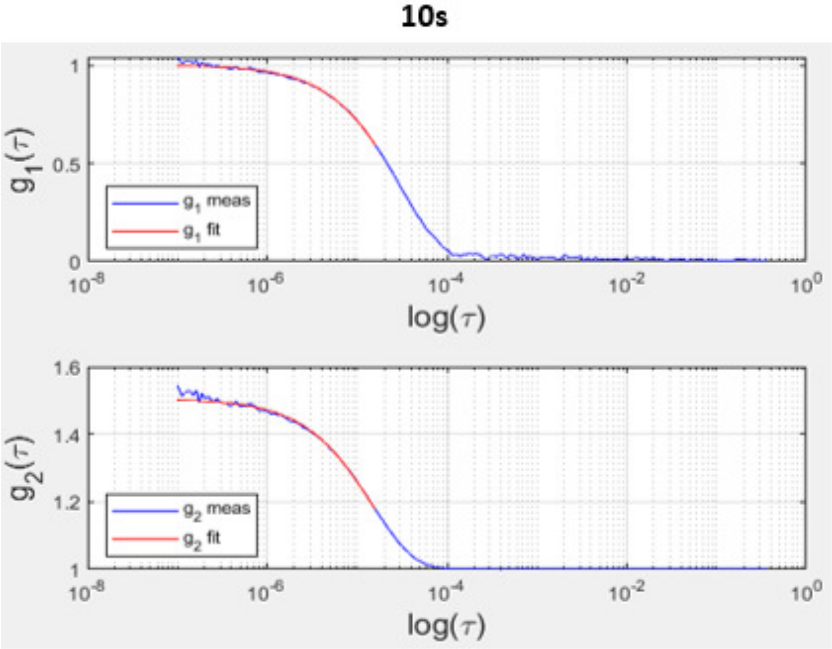

Figure 4.7 – Curves obtained, both g1 and g2 (blue) for a liquid phantom with different acquisition times of 1 second (top), 5 seconds (middle) and 10 seconds (below). Their respective fits are shown in red.

Figure 4.7 clearly shows that the fit for the liquid phantom is the best out of the three types of phantoms utilized. Not only are the curves exactly fitted for all cases, but also the decay of the curves can be seen to be happening before than the other phantoms, and the behavior at the very end of the curves is less chaotic than in the other cases as well.

Regarding the behavior of both D_B and β, Figure 4.8 shows that it is also way more controlled than for the other phantoms. Even though one can see clear variations among the values for each measured file, their range is a lot more defined, without the high peaks that are present in the previous cases. Not only that, but also as the acquisition time increases, the variation of the values decreases noticeably.

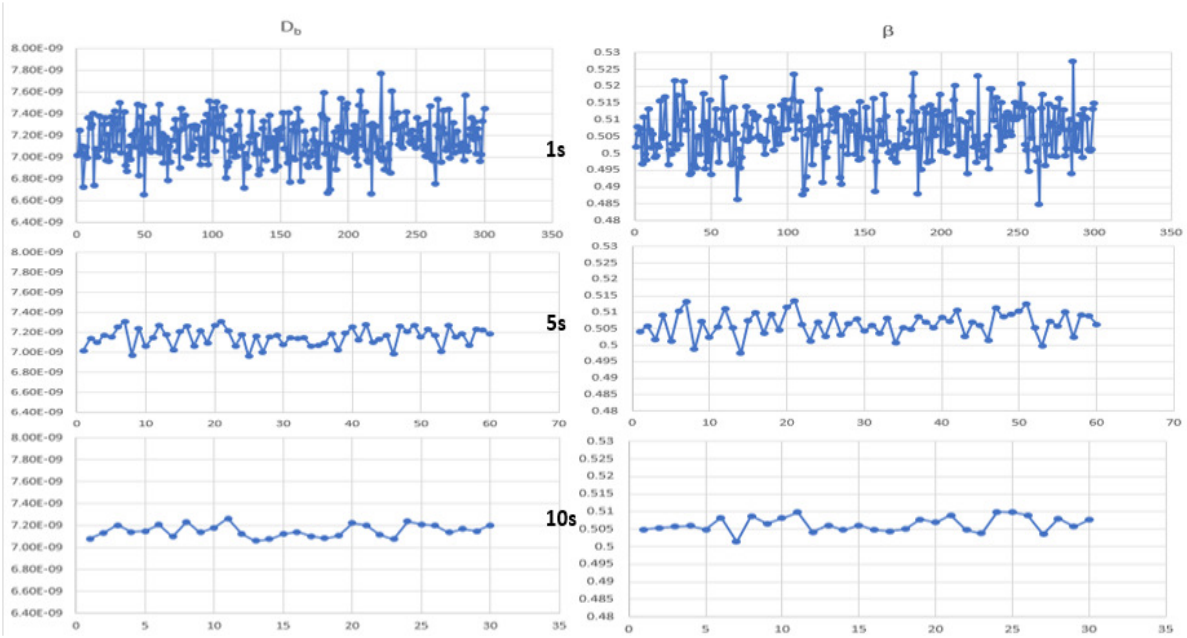

Figure 4.8 – Values obtained for D_B and β in different acquisition times of 1, 5, and 10 seconds for the liquid phantom.

The average values for both variables, along with their standard deviations, can be seen in the following table.

Table 4.3 – Average value and standard deviation of both D_B and β obtained for the liquid phantom.

	Average D_B	Average β	St. Dev. Of D_B	St. Dev. Of β
1s	7.16×10^{-9}	0.5063	1.926×10^{-10}	0.0072
5s	7.15×10^{-9}	0.5063	8.935×10^{-11}	0.0036
10s	7.15×10^{-9}	0.5063	5.574×10^{-11}	0.0021

Here in Table 4.3 one can observe that the values' behavior improves considerably with respect to the other cases. The standard deviation for the diffusion coefficient is smaller than the average in every case. On the other hand, β behaves as expected. The average value remains constant for every different acquisition time, and the standard deviation is greatly smaller than the average value, and it even diminishes as the acquisition time increases.

When comparing the graphs that group all of the obtained curves, the differences with the other phantoms can be immediately noticed, because for the liquid phantom there is almost no variation compared to the first phantoms. The curves overlap almost perfectly, and the range does not vary as wildly, if at all, when compared to the other cases. This is the behavior expected also from the other phantoms, which is clearly not achieved here.

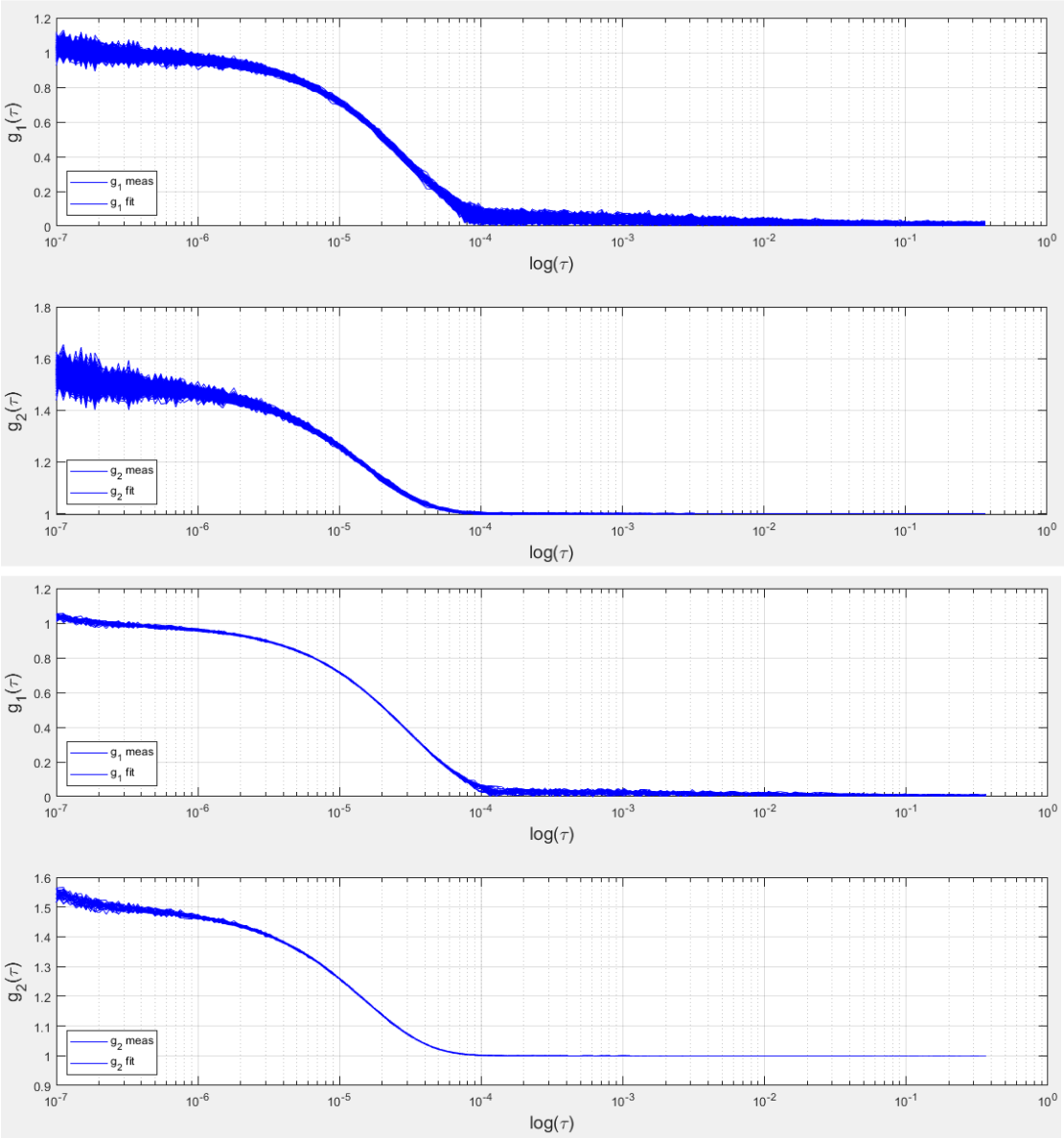

Figure 4.9 – All of the curves obtained for the liquid phantom are presented here (1 second case above, 10 second case below). The g_1 curves can be seen to overlap each other almost perfectly, with variations both at the beginning and the end of the curves. For g_2, the same behavior can be noticed, with the exception that the curves overlap also very well at the end. When going from 1 second to 10 seconds, this behavior can be seen even more notoriously.

4.4 Static background model implementation

The results shown so far have been utilizing the classical model that does not take into account the static background and the moving scatterers at the same time. In this section, an example of a comparison between the two models is shown.

First, in order to implement the new model, the MATLAB code was changed and tested to confirm that the results being obtained were consistent with the ones presented in the bibliography utilized to implement it, mainly [41]. The obtained results are shown in the next figure.

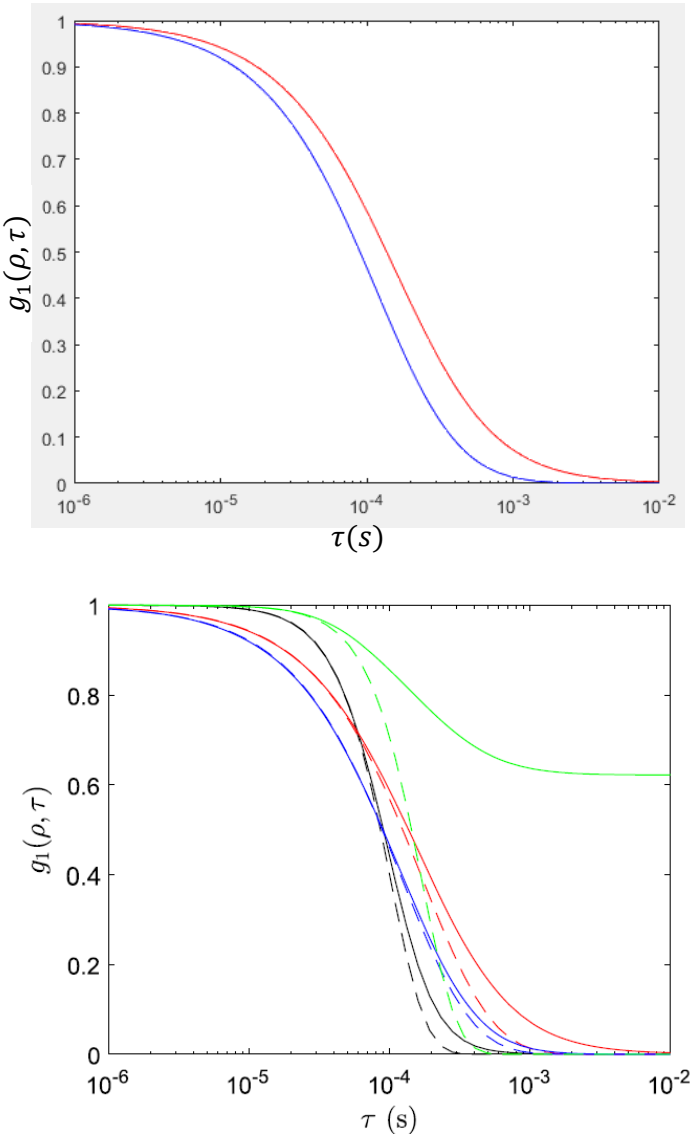

Figure 4.10 – Comparison between the new model implementation discussed in [41] (below) and the results obtained replicating the model in this work (above). All of the values utilized were the same as in [41]. Only two curves were replicated (their colors are the same in both figures) due to those being the only ones that utilized Brownian motion in [41], which is the motion used here. The other curves in the figure below are of no interest to this work. The graph depicted below has been directly obtained from [41].

One of the parameters that are introduced in the new model is P_m, which, as mentioned in chapter 2, is the probability that the scatterers are moving. This variable was left as a free parameter in this work, in order for it to be modified and observe how changing its value affected the obtained results. In the following figures, a comparison between both models is shown for the silicon phantom case.

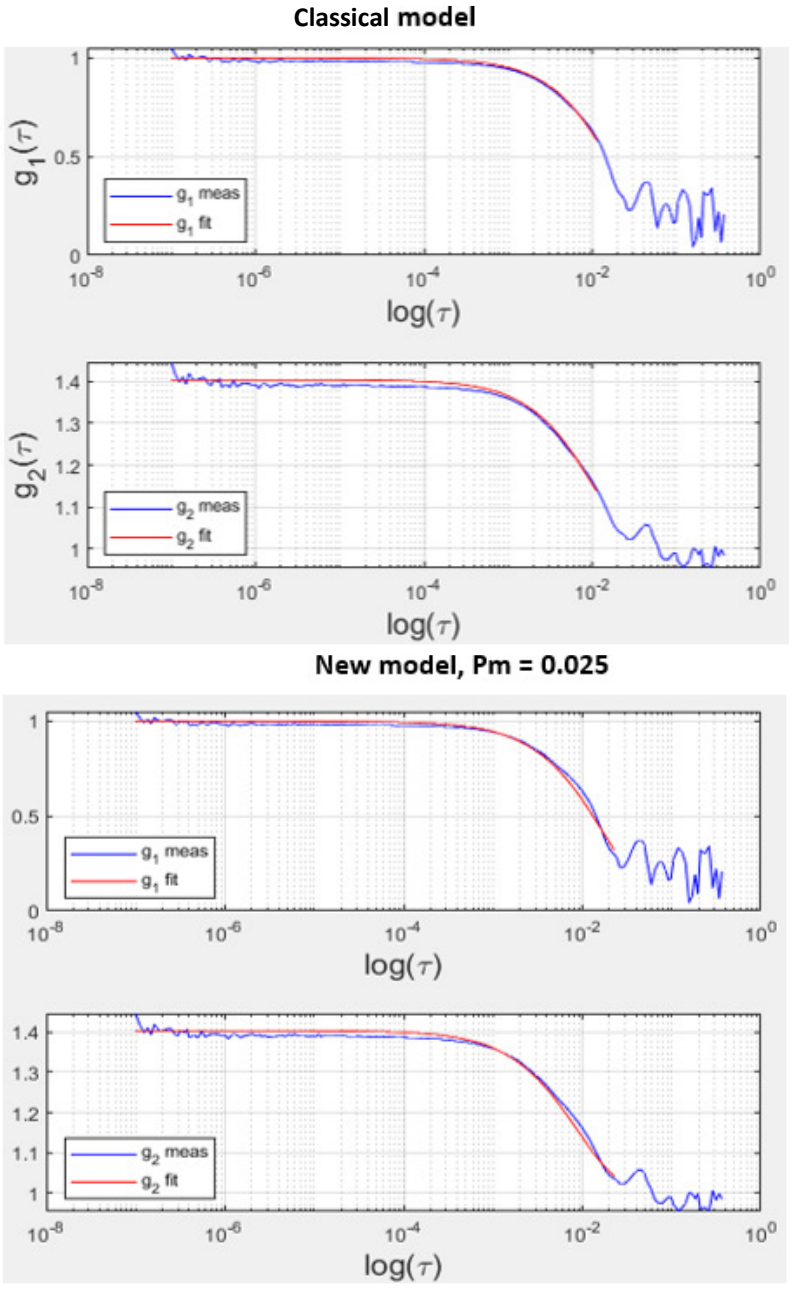

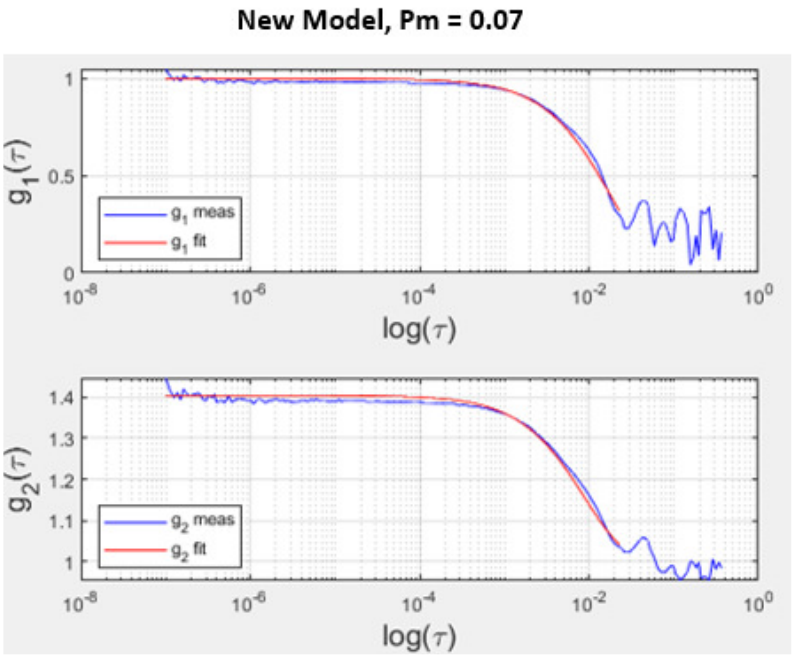

Figure 4.11 – A comparison between the classical model and the new model is shown here. The classical model (above) is compared against the new model with two different values for P_m: 0,025 (middle) and 0.07 (below).

It can be seen that there are actually no visible changes between the plots obtained. When comparing the values obtained for D_B and β, the only visible change seems to be the value of D_B, which increases greatly in the new model, and also as the value for P_m changes.

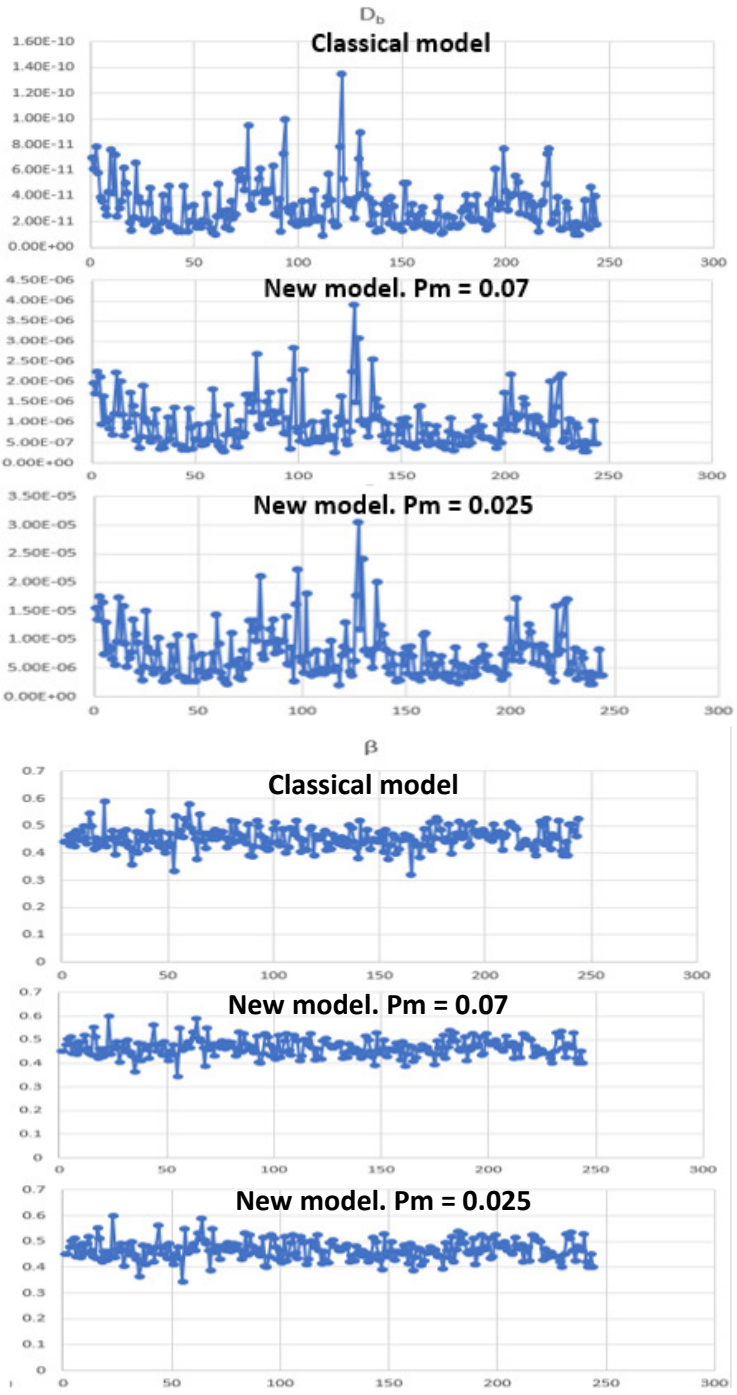

Figure 4.12 – Values obtained for D_B and β in both the classical and new models, with different values for Pm. Even though the behavior of the parameters is the same, the values for D_B change between models and also for different values of Pm. On the other hand, the β coefficient seems to remain unchanged.

Table 4.4 – Average value and standard deviation of both D_B and β obtained for the silicon phantom and for two different models.

	Average D_B	Average β	St. Dev. Of D_B	St. Dev. Of β
Classical Model	3.27×10^{-11}	0.457	1.934×10^{-11}	0.0395
$P_m = 0.07$	9.29×10^{-7}	0.467	5.527×10^{-7}	0.0394
$P_m = 0.025$	7.28×10^{-6}	0.467	4.333×10^{-6}	0.0394

More information can be obtained from Table 4.4, where it can be observed that the value for β remains practically unchanged, but the diffusion coefficient is notoriously modified both in terms of its average and its standard deviation.

In the following chapter, the results obtained for the analyzed fruits will be presented, and commented, in the same manner as in this one.

Chapter 5
Fruit Results

Having presented the results obtained for the phantoms, this chapter will now focus on the results obtained for different kinds of fruits. The methodology can be divided into two main paths:

- Study a group of different types of fruit and analyze the obtained results.
- Study a group of the same type of fruit to compare the obtained results between them.

The first methodology was done for two sets of different types of fruit: the first one was analyzed with two different interfiber distances (1 cm and 2.5 cm), and for the second one only one interfiber distance was used, equal to 1.5 cm. Both the classical model and the new model were used to analyze the results.

The second methodology was done for one group of fruit: apples. The interfiber distance was 2 cm. This group was first analyzed with the classic model, and then with the new model (both in the semi-infinite geometry). A brief comparison between models is shown in the following sections.

5.1 Groups with different types of fruit

There were two sets of measurements on different fruit analyzed for this section.

- The first set consisted of an aubergine, a lemon, an orange, a tangerine, a lime, and a tomato.
- The second set consisted of an aubergine, a lemon, an orange, a kiwi, and a tomato.

In both cases, 100 measurements were made with an acquisition time of 1 s each. Since two different interfiber distances were used for the first group, there are only 50 measurements available for each distance.

5.1.1 First set of measurements

This group was the first one analyzed overall during the realization of this thesis, so it was done with the objective of learning more about the response of the device when analyzing fruit in general. One of the main issues that arose in this set of measurements was that results for both the aubergine and lemon were unobtainable. In the aubergine case, this is thought to be because it has a dark purple, almost black, peel, which absorbs almost all the light which with it interacts. For the lemon, it is thought that this happened because of the thickness and rugosity of the peel, which is notoriously greater than the other fruit. Because of this, in the second group of fruit, discussed in the following section, a different approach to obtain the results was taken.

Regarding the other fruits, measurable data were obtained for the lime, the orange, tangerine, and the tomato.

Lime

In the following figure, a comparison between the curves obtained for each interfiber distance can be observed. The difference in the fit between both distances is noteworthy. The 1 cm case works very well, while the 2.5 cm distance shows a bad fit.

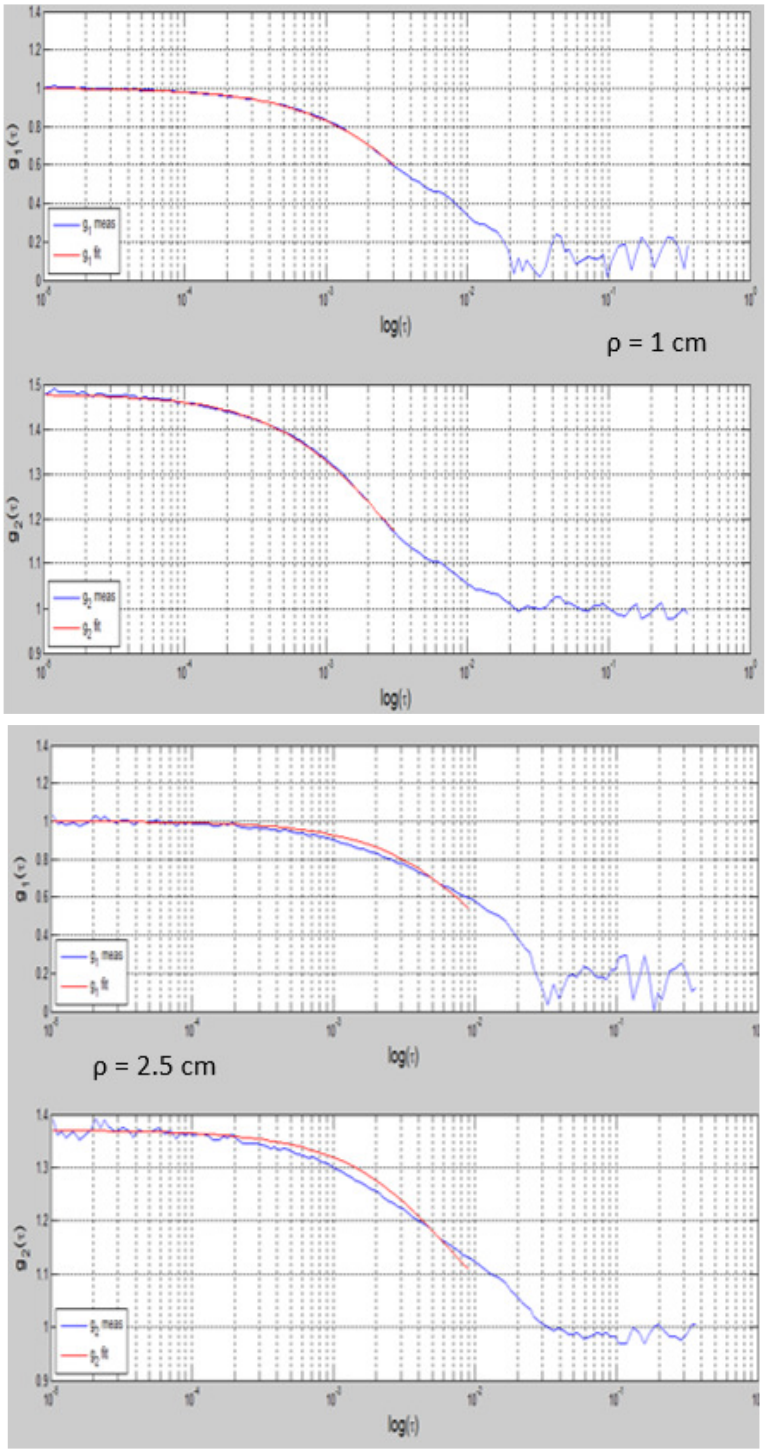

Figure 5.1 – Comparison between the curves obtained for a lime with two different interfiber distances: 1 cm (above) and 2.5 cm (below).

The value of the diffusion coefficient, D_B, is presented in the following graphs.

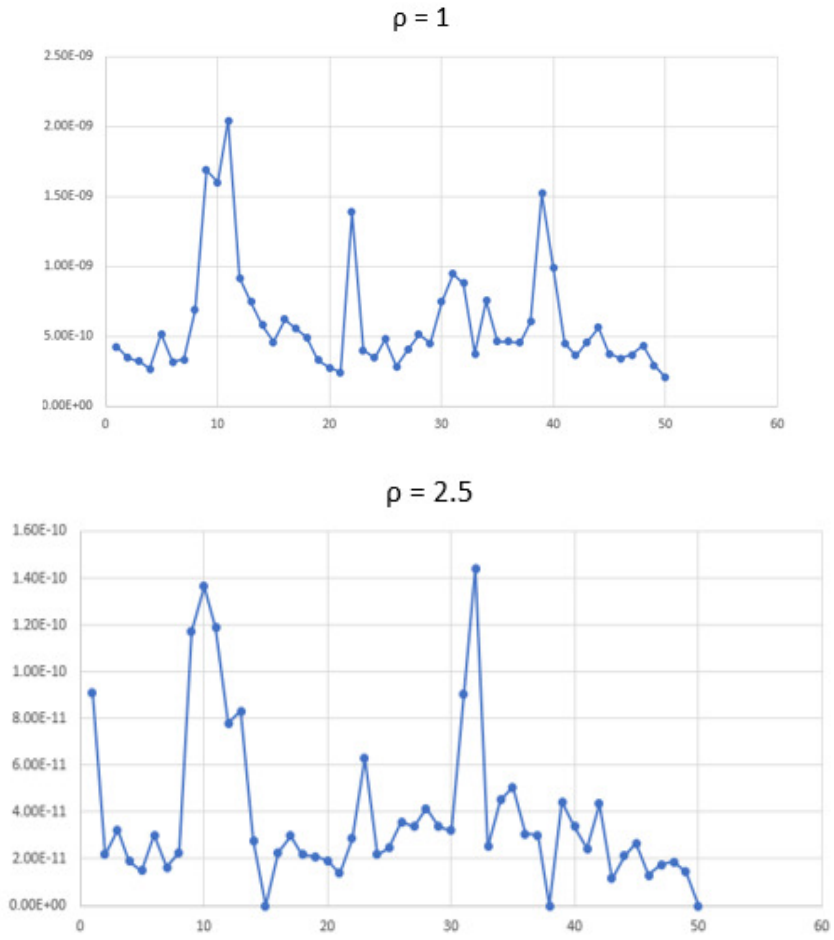

Figure 5.2 – Values for the diffusion coefficient of a lime obtained for two interfiber distances (in cm).

The most noticeable change is the value of D_B in each case. It changes by an order of magnitude between each interfiber distance (see Table 5.1). Its behaviour, on the other hand, fluctuates a lot in both cases. Another change that can be observed is that of β, which diminishes as the interfiber distance increases.

Table 5.1 – Average value and standard deviation of both D_B and β obtained for a lime, using two different interfiber distances.

ρ	Average D_B	St. Dev. Of D_B	Average of β	St. Dev. Of β
1 cm	6.005×10^{-10}	4.044×10^{-10}	0.460	0.0184
2.5 cm	4.129×10^{-11}	3.341×10^{-11}	0.421	0.0386

As it can be seen in Table 5.1, the value of the diffusion coefficient has a standard deviation that is very close to the value of its average. This is not good, as it should be much lower.

This seems to be a repeating tendency in the results obtained throughout this work for both fruit and phantoms.

Orange

Results obtained for the orange follow a similar behavior as the ones obtained for the lime. The same comments can be made: the fit works much better for the shorter interfiber distance.

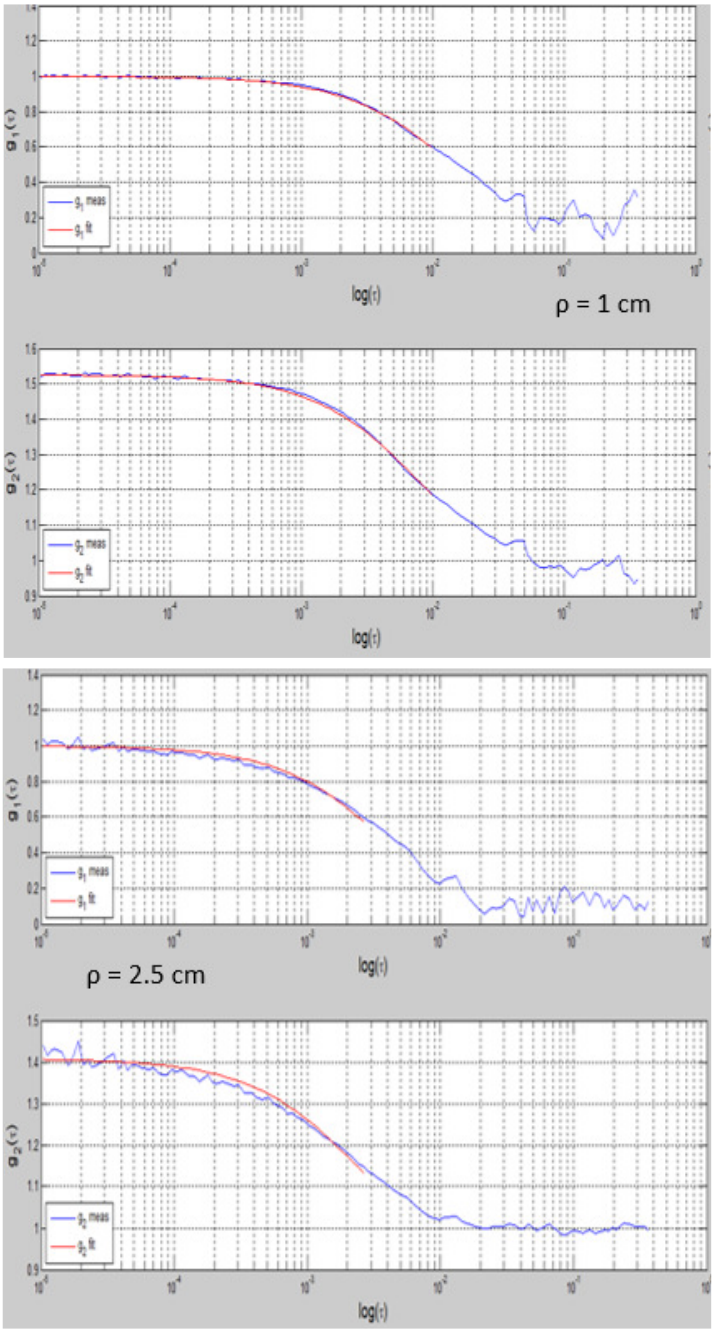

Figure 5.3 – Comparison between the curves obtained for an orange with two different interfiber distances: 1 cm (above) and 2.5 cm (below).

Now, for the diffusion coefficient:

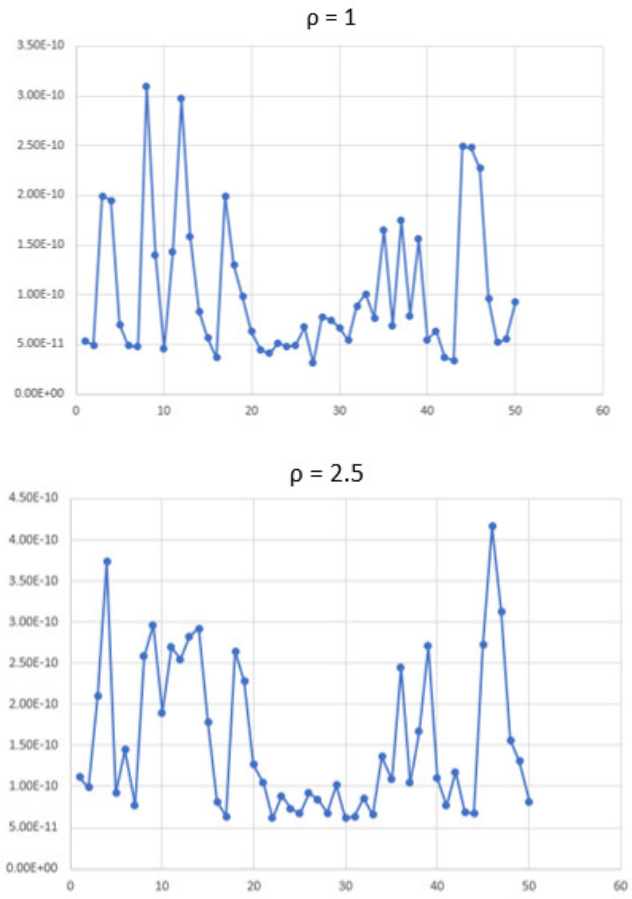

Figure 5.4 – Values for the diffusion coefficient of an orange obtained for two interfiber distances (in cm).

In this case depicted in Figure 5.4, the value of the diffusion coefficient fluctuates a lot, but around the same order of magnitude for both interfiber distances. It does not have a variation as big as the one in the lime.

Table 5.2 – Average value and standard deviation of both D_B and β obtained for an orange, using two different interfiber distances.

ρ	Average D_B	St. Dev. Of D_B	Average of β	St. Dev. Of β
1 cm	1.027×10^{-10}	7.235×10^{-11}	0.452	0.0373
2.5 cm	1.550×10^{-10}	9.392×10^{-11}	0.410	0.0204

Table 5.2 shows that the values obtained for the diffusion coefficient go more in line with what is expected: mainly the fact that the standard deviation is much lower than the average of the value. Also, the change in the value obtained for each interfiber distance is not big, probably due to the shiner peel. On the other side, the behavior of the β coefficient is similar to the one in the lime before: it diminishes as the interfiber distance increases.

Tangerine

The tendency in the results continues with the ones obtained for the tangerine.

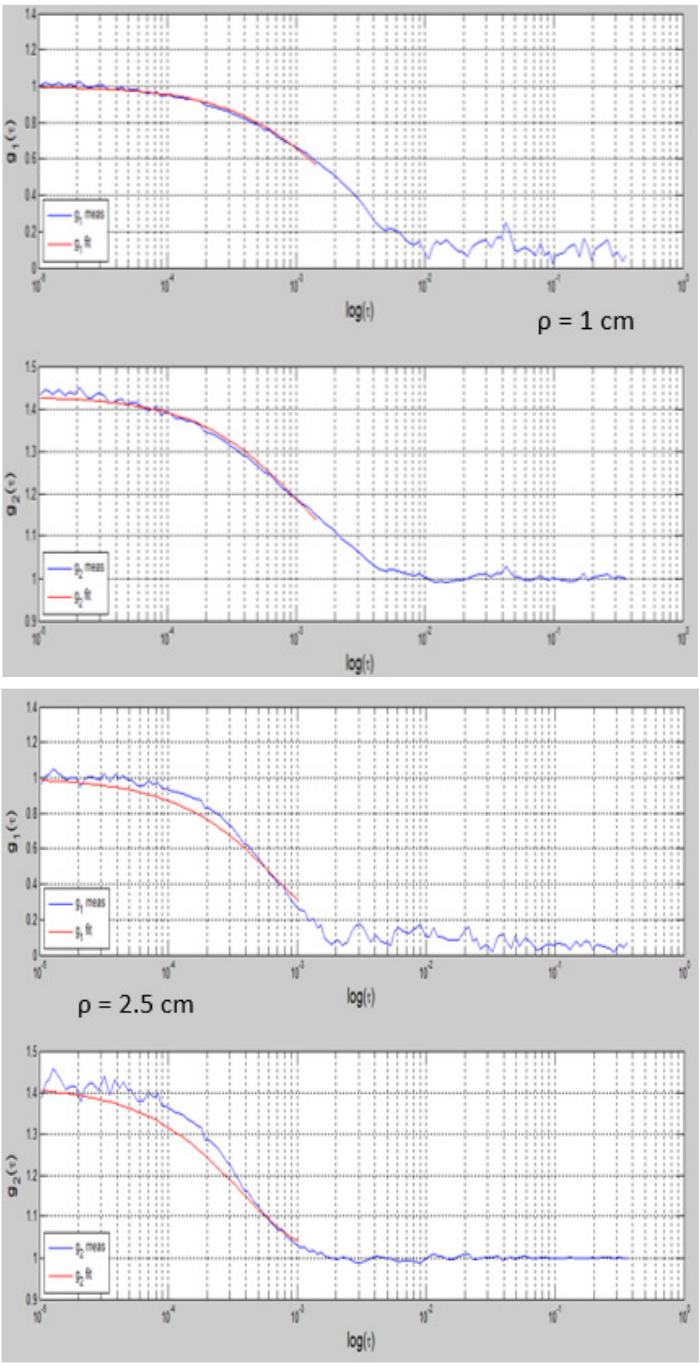

Figure 5.5 – Comparison between the curves obtained for a tangerine with two different interfiber distances: 1 cm (above) and 2.5 cm (below).

Just as with the rest of the fruit so far, the fit works better for the shorter interfiber distance, but in this case, it is not as perfect as it was in the previous ones. Surprisingly, when considering the value of the diffusion coefficient, there is a huge change of behavior between each interfiber distance, as it can be seen in Figure 5.6

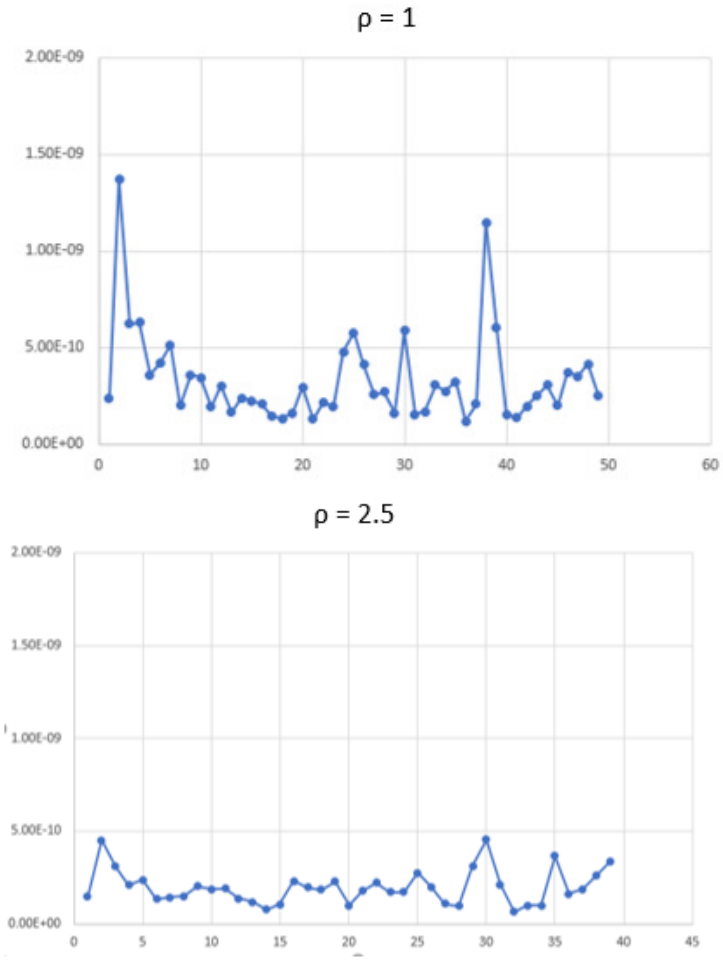

Figure 5.6 – Values for the diffusion coefficient of a tangerine obtained for two interfiber distances (in cm).

When the interfiber distance is 2.5 cm, the diffusion coefficient does not fluctuate as much as for the 1 cm case. This can be a good sign to consider when utilizing this distance, but evaluating the average and standard deviation of these values, as shown in Table 5.3, may lead to a different conclusion.

Table 5.3 – Average value and standard deviation of both D_B and β obtained for a tangerine, using two different interfiber distances.

ρ	Average D_B	St. Dev. Of D_B	Average of β	St. Dev. Of β
1 cm	3.290×10^{-10}	2.391×10^{-10}	0.461	0.0236
2.5 cm	4.015×10^{-10}	6.66×10^{-10}	0.409	0.0174

The standard deviation of the diffusion coefficient is enormous, even bigger than its own average value in case of the 2.5 cm distance. This makes the results obtained completely unreliable. On the other hand, the values obtained for β indicate the same behaviour present in the past two fruits.

Tomato

The case of the tomato can be seen in the following figures.

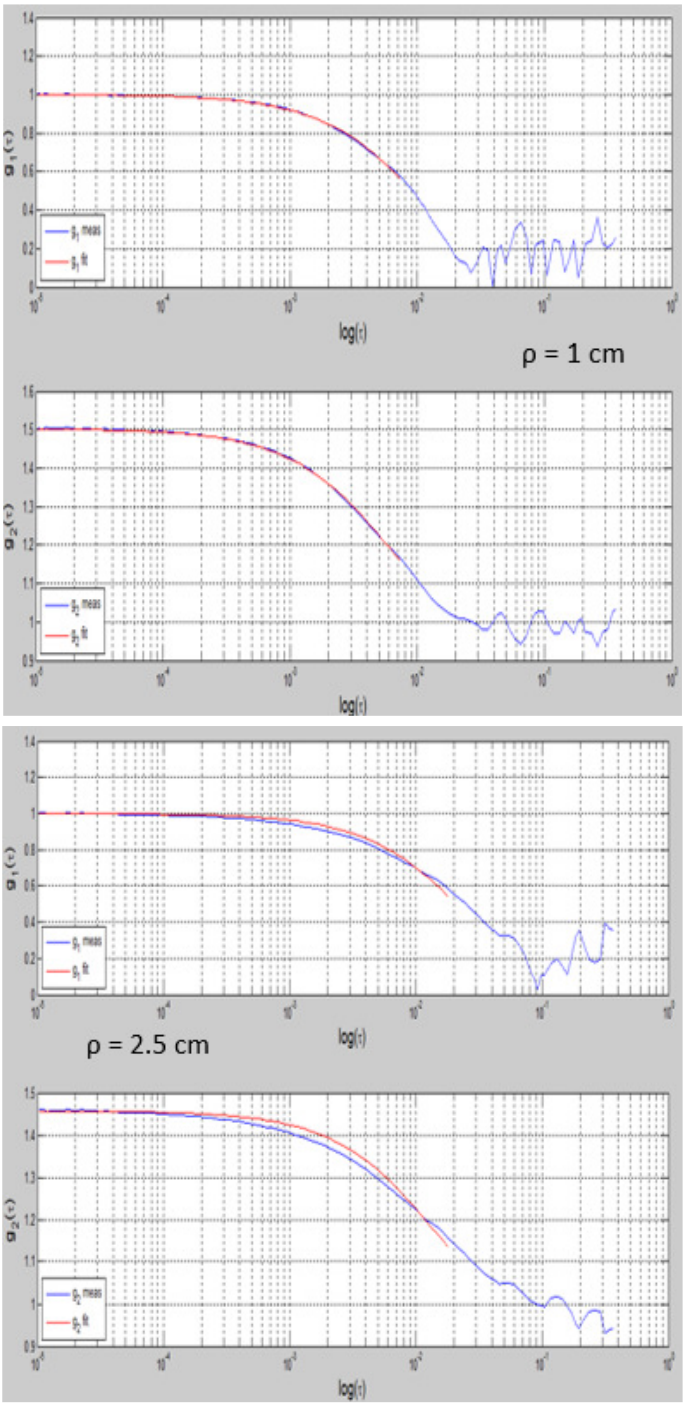

Figure 5.7 – Comparison between the curves obtained for a tomato with two different interfiber distances: 1 cm (above) and 2.5 cm (below).

The same behavior in the fit is observed, just like with the past fruits. The diffusion coefficient's behavior is shown next.

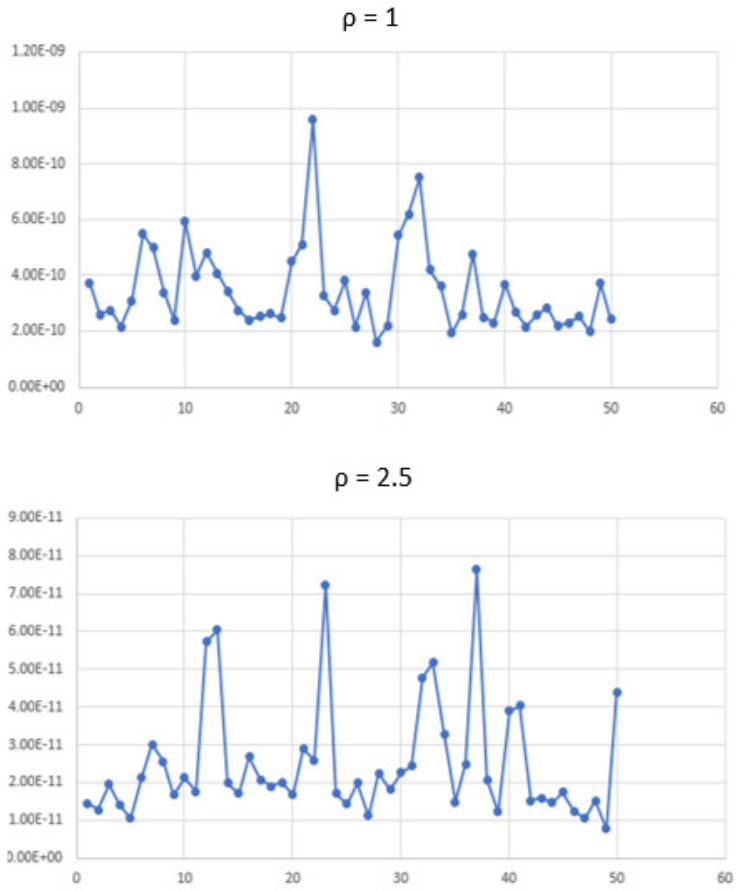

Figure 5.8 – Values for the diffusion coefficient of a tomato obtained for two interfiber distances (in cm).

Again, the values' variation is considerable between both interfiber distances, it is of more than an order of magnitude, which is further shown in the Table 5.4. The value of β diminishes as the interfiber distance increases, as before.

Table 5.4 – Average value and standard deviation of both D_B and β obtained for a tomato, using two different interfiber distances.

ρ	Average D_B	St. Dev. Of D_B	Average β	St. Dev. Of β
1 cm	3.483×10^{-10}	1.552×10^{-10}	0.466	0.0202
2.5 cm	2.507×10^{-11}	1.574×10^{-11}	0.460	0.0421

In the end, the diffusion coefficient again varies very much, in a similar manner to the lime, where the values between interfiber distances change around one order of magnitude. The

standard deviation is again very close to the average value, which, as said before, is neither good nor expected.

An attempt to improve the obtained results was made with the second group of fruit, presented in the following section.

5.1.2 Second set of measurements

This group was the last one analyzed overall during the realization of this thesis, so it was done with the objective of improving the results obtained with the first group, mentioned in the past section. One of the main differences implemented during the experimentation with this group of fruit was that the measurements were done twice: once for the fruits with peel, and once with the fruits cut in half, so that the probe was placed straight on the interior of the fruits. This was done to see if the results improved, mainly in the cases of the aubergine and lemon, which were impossible to analyze the first time. On the other hand, a kiwi was utilized, because they are highly juicy.

In this group, the interfiber distance was always the same, fixed at 1.5 cm. All data were analyzed with the new model, with two different values for P_m: 0.025 and 0.001.

Generally, for all the fruit analyzed here, there were some cases in which the fitting curves worked very well for some data, and then did not work at all for other data. There was not a constant, or repetitive tendency of the results. This can be observed in the following figure.

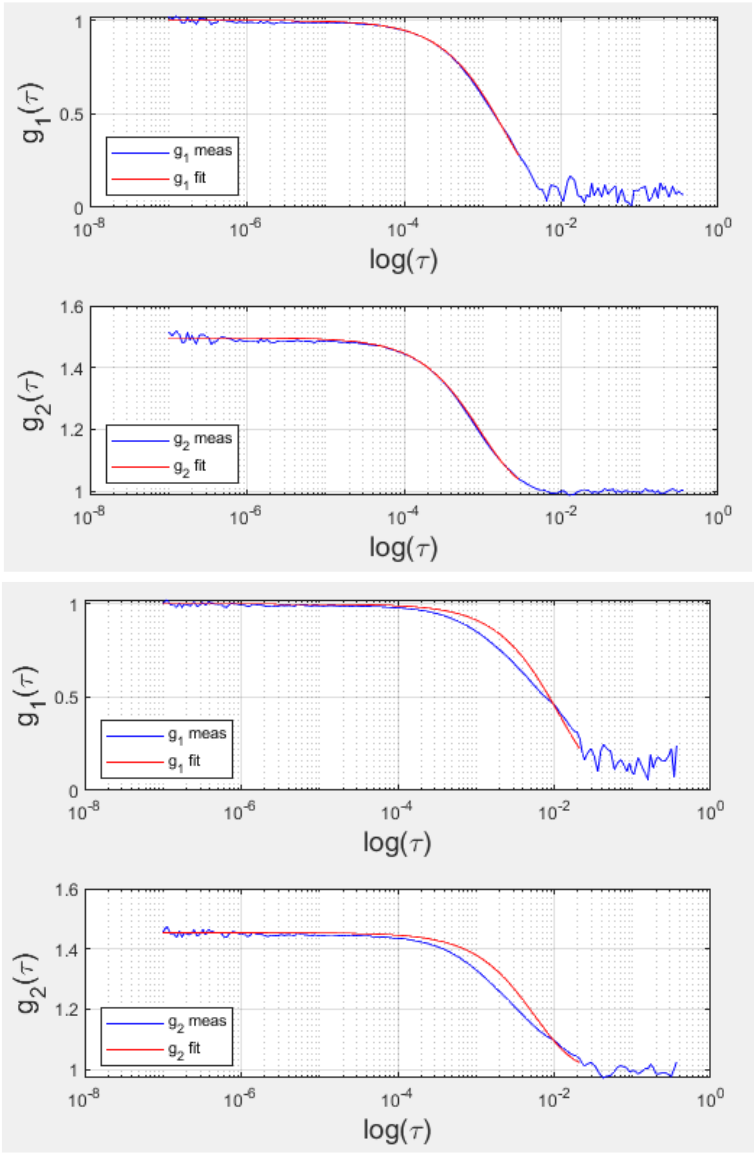

Figure 5.9 – Fitting curves obtained for a tomato without peel at different points in time. P_m value = 0.025.

Figure 5.9 shows the curves obtained for a tomato without peel at different points in time. It is clearly seen that the curves depicted above fit the data very well, while the ones below do not. This happened with all the analyzed fruit, regardless of them having peel or not.

Comparing the data obtained by using different acquisition times (just like in the last section) of 1, 5, and 10 seconds, was also not conclusive enough. For some fruit, like the orange, a clear improvement can be seen as this time increases, while for other fruit, like the aubergine without a peel, there was no improvement at all. The following graphs depict this case for the orange. In them, a slight improvement in the fitting curves can be observed as the acquisition time increases.

1s

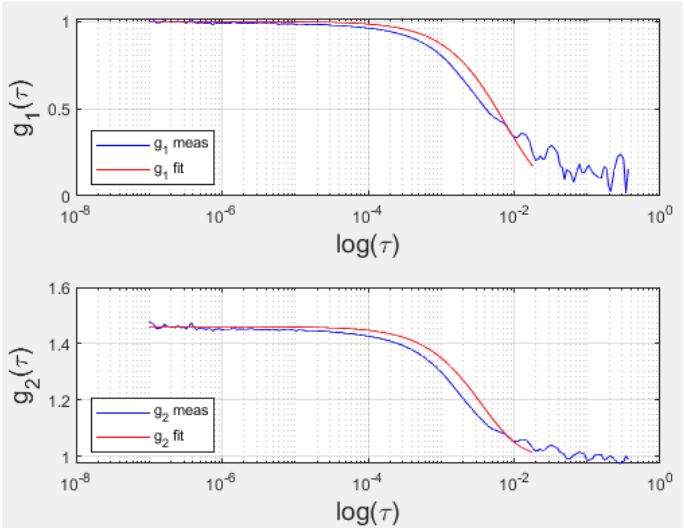
$g_1(\tau)$
g_1 meas
g_1 fit
log(τ)
$g_2(\tau)$
g_2 meas
g_2 fit
log(τ)

5s

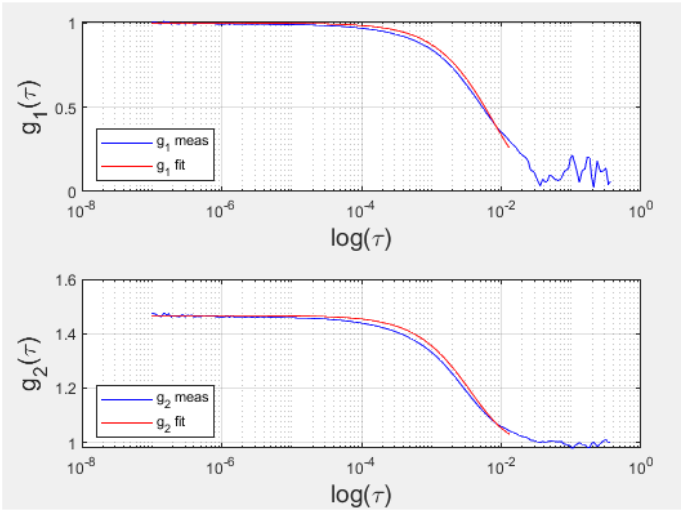
$g_1(\tau)$
g_1 meas
g_1 fit
log(τ)
$g_2(\tau)$
g_2 meas
g_2 fit
log(τ)

10s

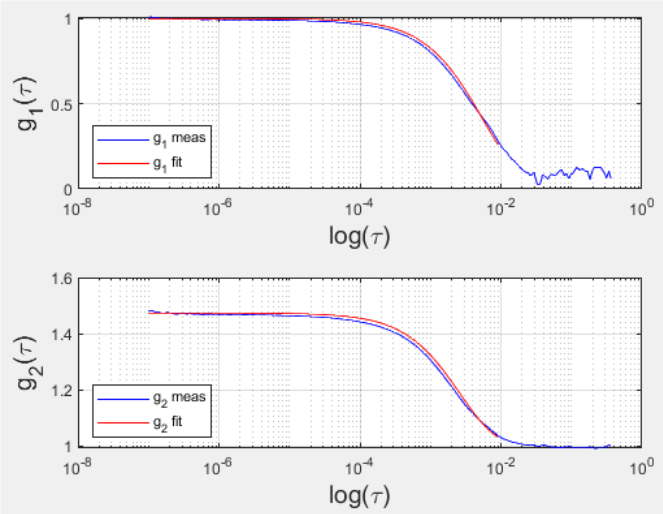

Figure 5.10 – Fitting curves obtained for an orange (with peel) for different acquisition times of 1, 5, and 10 seconds respectively. P_m value = 0.025.

For other fruits, though, this was not the case. The following graphs depict the same curves but for an aubergine without peel.

1s

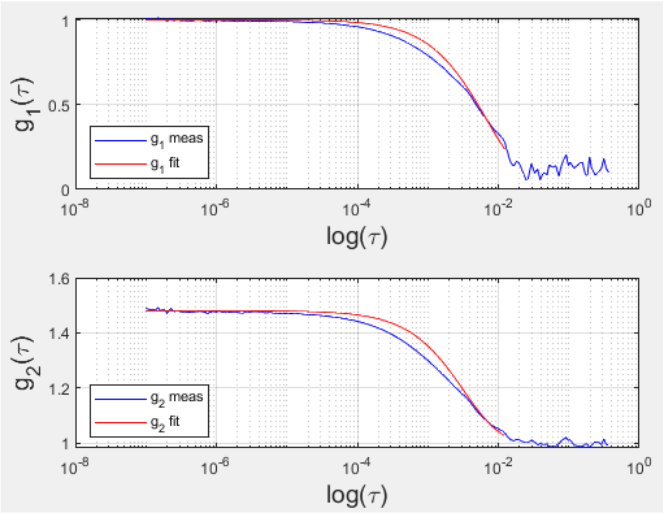

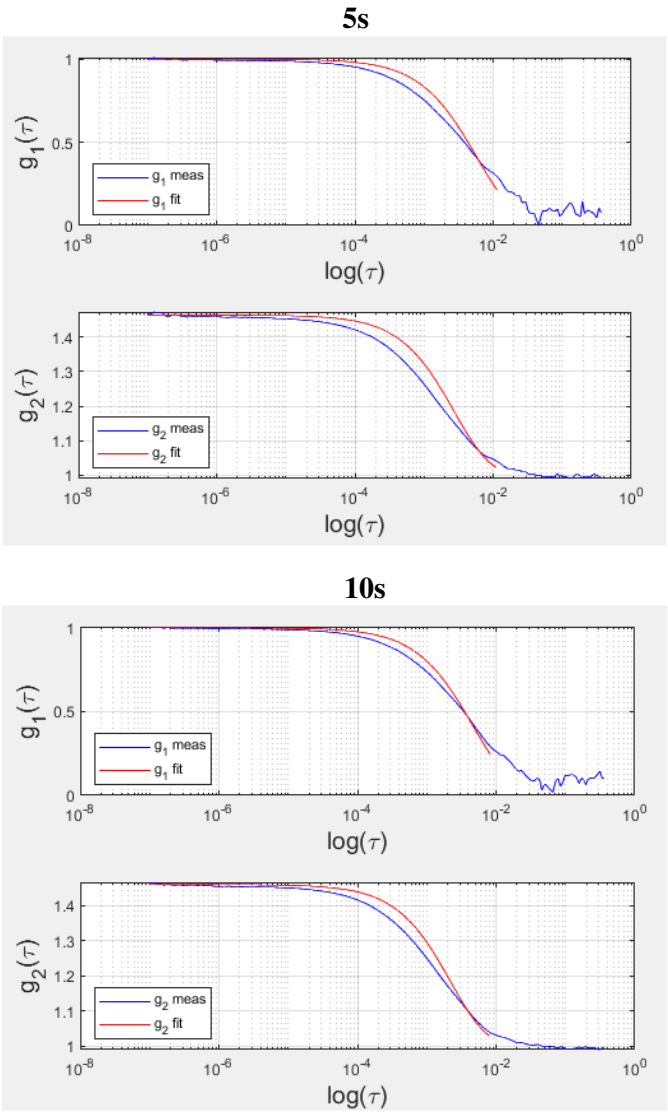

Figure 5.11 – Fitting curves obtained for an aubergine (without peel) for different acquisition times of 1, 5, and 10 seconds respectively. P_m value = 0.025.

As mentioned before, in the aubergine case there is no general improvement as the acquisition time increases. This was the general case for the other fruits analyzed too.

One thing that was achieved, though, was obtaining results for both the lemon and the aubergine. They were not good enough, as has been the case in general for the rest of the fruit. The fitting curves will fit the data sometime, and the next moment they will not, just like with the example shown in Figure 5.9 for the tomato. The same thing happened with the kiwi, and in general for all the fruits when they were analyzed with and without peel.

However, there is one interesting observation that can be done with the obtained results, which is how changing the value of P_m affected the value for the diffusion coefficient.

This can be analyzed by directly checking the values obtained for the diffusion coefficient, D_B. These values changed considerably whenever the P_m variable was modified. This is shown in Figure 5.12, using the orange with peel as an example.

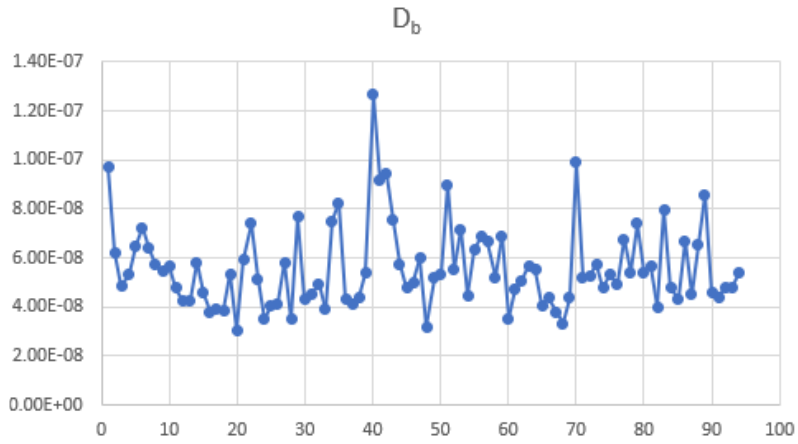

(a) – Values obtained for the diffusion coefficient in an orange with peel for a time = 1s, and $P_m = 0.025$.

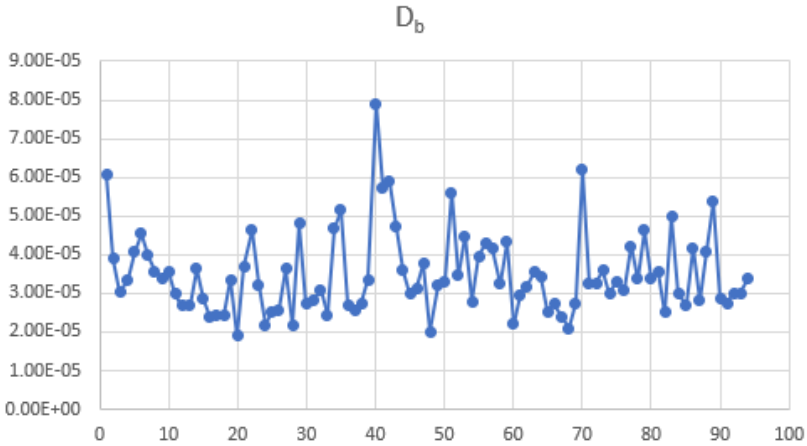

(b) – Values obtained for the diffusion coefficient in an orange with peel for a time = 1s, and $P_m = 0.001$.

5.12 – Comparison between the values obtained for the diffusion coefficient of an orange with peel for different values of P_m.

It can be observed that the behavior of the diffusion coefficient is exactly the same in both cases depicted in Figure 5.12, but as P_m decreased, the values obtained changed considerably, increasing around two or three orders of magnitude. This change was observed for every single case that was evaluated. The average values obtained for both D_B and β, along with their respective standard deviations, are included in Table 5.5.

Table 5.5 – Average value and standard deviation of both D_B and β obtained for the different fruits analyzed in this section, with and without peel.

Orange (peel)	Average D_B	Average β	St. Dev. Of D_B	St. Dev. Of β
1s, $P_m = 0.025$	5.47×10^{-8}	0.468	1.73×10^{-8}	0.021
1s, $P_m = 0.001$	3.42×10^{-5}	0.468	1.07×10^{-5}	0.021
5s, $P_m = 0.025$	5.24×10^{-8}	0.469	5.80×10^{-9}	0.007
5s, $P_m = 0.001$	3.28×10^{-5}	0.469	4.27×10^{-6}	0.008
10s, $P_m = 0.025$	5.25×10^{-8}	0.469	6.84×10^{-9}	0.008
10s, $P_m = 0.001$	3.28×10^{-5}	0.469	3.62×10^{-6}	0.007

Orange (no peel)	Average D_B	Average β	St. Dev. Of D_B	St. Dev. Of β
1s, $P_m = 0.025$	5.82×10^{-8}	0.471	4.53×10^{-8}	0.024
1s, $P_m = 0.001$	3.63×10^{-5}	0.471	2.83×10^{-5}	0.024
5s, $P_m = 0.025$	5.03×10^{-8}	0.471	1.72×10^{-8}	0.011
5s, $P_m = 0.001$	3.14×10^{-5}	0.471	1.07×10^{-5}	0.011
10s, $P_m = 0.025$	4.91×10^{-8}	0.471	1.26×10^{-8}	0.008
10s, $P_m = 0.001$	3.07×10^{-5}	0.471	7.86×10^{-6}	0.008

Kiwi (peel)	Average D_B	Average β	St. Dev. Of D_B	St. Dev. Of β
1s, $P_m = 0.025$	2.28×10^{-7}	0.463	2.26×10^{-7}	0.037
1s, $P_m = 0.001$	1.42×10^{-4}	0.463	1.41×10^{-4}	0.037
5s, $P_m = 0.025$	1.96×10^{-7}	0.463	7.54×10^{-8}	0.015
5s, $P_m = 0.001$	1.22×10^{-4}	0.463	4.71×10^{-5}	0.015
10s, $P_m = 0.025$	1.95×10^{-7}	0.463	7.09×10^{-8}	0.007
10s, $P_m = 0.001$	1.21×10^{-4}	0.463	4.43×10^{-5}	0.007

Kiwi (no peel)	Average D_B	Average β	St. Dev. Of D_B	St. Dev. Of β
1s, $P_m = 0.025$	1.21×10^{-7}	0.476	8.21×10^{-8}	0.034
1s, $P_m = 0.001$	7.58×10^{-5}	0.476	5.13×10^{-5}	0.034
5s, $P_m = 0.025$	1.07×10^{-7}	0.477	2.08×10^{-8}	0.016
5s, $P_m = 0.001$	6.70×10^{-5}	0.477	1.30×10^{-5}	0.016
10s, $P_m = 0.025$	1.06×10^{-7}	0.477	1.71×10^{-8}	0.011

10s, P_m = 0.001	$6.62x10^{-5}$	0.477	$1.07x10^{-5}$	0.011

Lemon (peel)	Average D_B	Average β	St. Dev. Of D_B	St. Dev. Of β
1s, P_m = 0.025	$4.15x10^{-8}$	0.461	$2.21x10^{-8}$	0.033
1s, P_m = 0.001	$2.59x10^{-5}$	0.461	$1.38x10^{-5}$	0.033
5s, P_m = 0.025	$3.69x10^{-8}$	0.460	$9.86x10^{-9}$	0.016
5s, P_m = 0.001	$2.31x10^{-5}$	0.460	$6.16x10^{-6}$	0.016
10s, P_m = 0.025	$3.63x10^{-8}$	0.460	$7.16x10^{-9}$	0.012
10s, P_m = 0.001	$2.27x10^{-5}$	0.460	$4.47x10^{-6}$	0.012

Lemon (no peel)	Average D_B	Average β	St. Dev. Of D_B	St. Dev. Of β
1s, P_m = 0.025	$2.88x10^{-7}$	0.454	$2.35x10^{-7}$	0.032
1s, P_m = 0.001	$1.80x10^{-4}$	0.454	$1.47x10^{-4}$	0.032
5s, P_m = 0.025	$2.38\ x10^{-7}$	0.455	$9.14x10^{-8}$	0.012
5s, P_m = 0.001	$1.48x10^{-4}$	0.455	$5.72x10^{-5}$	0.012
10s, P_m = 0.025	$2.31x10^{-7}$	0.455	$6.83x10^{-8}$	0.006
10s, P_m = 0.001	$1.45x10^{-4}$	0.455	$4.27x10^{-5}$	0.006

Aubergine (peel)	Average D_B	Average β	St. Dev. Of D_B	St. Dev. Of β
1s, P_m = 0.025	$6.63x10^{-8}$	0.476	$5.60x10^{-8}$	0.020
1s, P_m = 0.001	$4.14x10^{-5}$	0.476	$3.50x10^{-5}$	0.020
5s, P_m = 0.025	$6.08x10^{-8}$	0.476	$1.99x10^{-8}$	0.009
5s, P_m = 0.001	$3.80x10^{-5}$	0.476	$1.24x10^{-5}$	0.009
10s, P_m = 0.025	$5.88x10^{-8}$	0.476	$1.07x10^{-8}$	0.006
10s, P_m = 0.001	$3.67x10^{-5}$	0.476	$6.71x10^{-6}$	0.006

Aubergine (no peel)	Average D_B	Average β	St. Dev. Of D_B	St. Dev. Of β
1s, P_m = 0.025	$4.95x10^{-8}$	0.465	$3.03x10^{-8}$	0.020
1s, P_m = 0.001	$3.10x10^{-5}$	0.465	$1.89x10^{-5}$	0.020
5s, P_m = 0.025	$4.53x10^{-8}$	0.465	$1.08x10^{-8}$	0.008
5s, P_m = 0.001	$2.83x10^{-5}$	0.465	$6.73x10^{-6}$	0.008

10s, $P_m = 0.025$	4.48×10^{-8}	0.465	7.19×10^{-9}	0.006
10s, $P_m = 0.001$	2.80×10^{-5}	0.465	4.49×10^{-6}	0.006

Tomato (peel)	Average D_B	Average β	St. Dev. Of D_B	St. Dev. Of β
1s, $P_m = 0.025$	1.33×10^{-6}	0.454	2.16×10^{-6}	0.040
1s, $P_m = 0.001$	8.30×10^{-4}	0.454	1.35×10^{-3}	0.040
5s, $P_m = 0.025$	7.69×10^{-7}	0.454	3.88×10^{-7}	0.020
5s, $P_m = 0.001$	4.80×10^{-4}	0.454	2.42×10^{-4}	0.020
10s, $P_m = 0.025$	7.07×10^{-7}	0.454	2.06×10^{-7}	0.017
10s, $P_m = 0.001$	4.42×10^{-4}	0.454	1.29×10^{-4}	0.017

Tomato (no peel)	Average D_B	Average β	St. Dev. Of D_B	St. Dev. Of β
1s, $P_m = 0.025$	3.68×10^{-7}	0.473	4.82×10^{-7}	0.029
1s, $P_m = 0.001$	2.30×10^{-4}	0.473	3.01×10^{-4}	0.029
5s, $P_m = 0.025$	2.71×10^{-7}	0.475	1.77×10^{-7}	0.012
5s, $P_m = 0.001$	1.70×10^{-4}	0.475	1.11×10^{-4}	0.012
10s, $P_m = 0.025$	2.32×10^{-7}	0.475	7.32×10^{-8}	0.010
10s, $P_m = 0.001$	1.45×10^{-4}	0.475	4.57×10^{-5}	0.010

There are a few comments that can be made by observing the data from the table above.

- As the value of P_m decreases, the value of the diffusion coefficient increases, but the value of β stays practically unchanged.
- The results vary wildly between different types of fruit or even between the same type with and without the peel (see the lemon, for example).
- Both D_B and β change very little when increasing the acquisition time.
- The results obtained for some fruits are not possible to trust at all, due to the fact that their standard deviation is very close, or even bigger, than the value of the average. This can be seen, for example, in the tomato without peel or in the kiwi with peel.
- The standard deviation of the diffusion coefficient tends to improve as the acquisition time increases.

Another important thing worthy of mentioning is that in this group of fruit, when the aubergine and the lemon were analyzed with the peel, before cutting them in half, results

were actually obtained, they were not as bad as during the first attempt, but they were also not good in general. In the table above their values for the diffusion coefficient and β are still included for completeness.

5.2 Group of apples

A group of five apples was analyzed to compare the results obtained between them. Three apples were of the same kind, while the other two were of different kinds, to also see if there were any type of changes between the results for different kinds of apples. Also, both models were used to analyze some of the apples' data to compare them too.

As it has been mentioned at the beginning of the chapter, the interfiber distance used for this group was fixed at 2 cm. A total of 300 measurements with an acquisition time of 1 second were taken for each apple.

The results obtained followed the same tendency as with the rest of the fruit presented here so far: some of the curves fitted well, and some did not. To be more concise, and to avoid repetition, the results shown here will only be a comparison both between apples and models.

5.2.1 Comparison between apples

The values obtained for the diffusion coefficient of different apples are shown in the following.

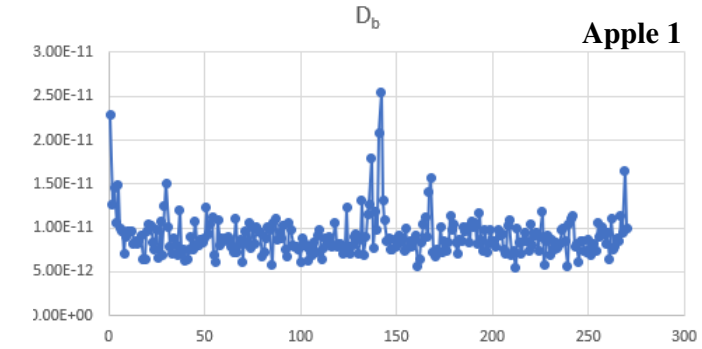
D_b
Apple 1
3.00E-11
2.50E-11
2.00E-11
1.50E-11
1.00E-11
5.00E-12
0.00E+00
0
50
100
150
200
250
300

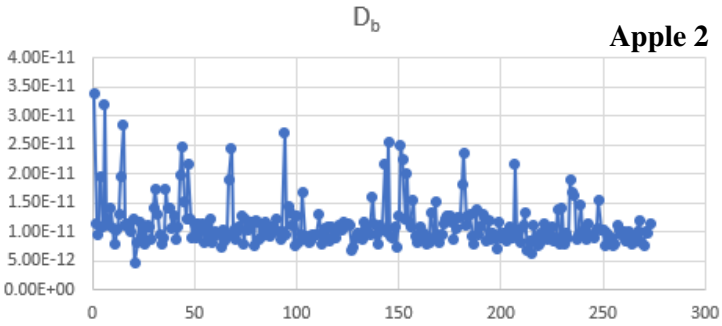
D_b
Apple 2
4.00E-11
3.50E-11
3.00E-11
2.50E-11
2.00E-11
1.50E-11
1.00E-11
5.00E-12
0.00E+00
0
50
100
150
200
250
300

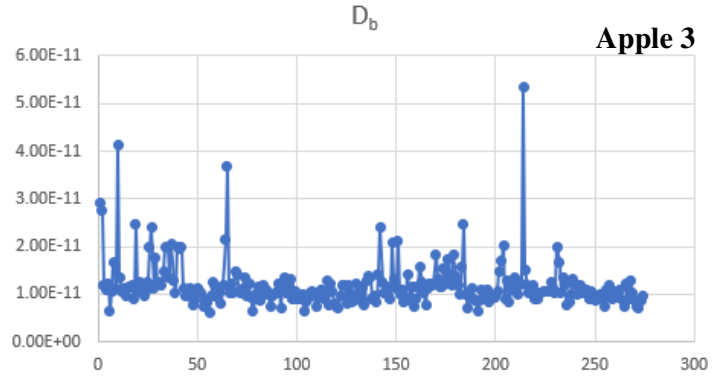
D_b
Apple 3
6.00E-11
5.00E-11
4.00E-11
3.00E-11
2.00E-11
1.00E-11
0.00E+00
0
50
100
150
200
250
300

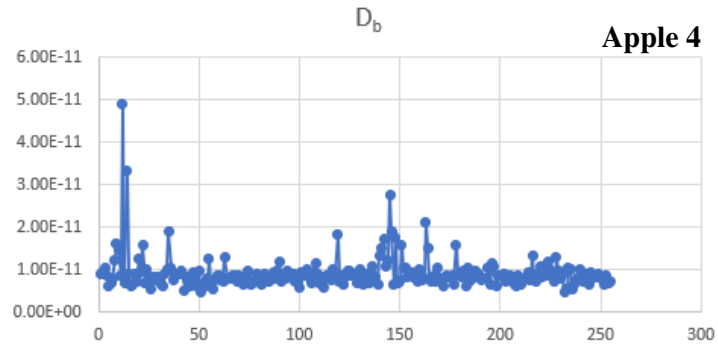
D_b
Apple 4
6.00E-11
5.00E-11
4.00E-11
3.00E-11
2.00E-11
1.00E-11
0.00E+00
0
50
100
150
200
250
300

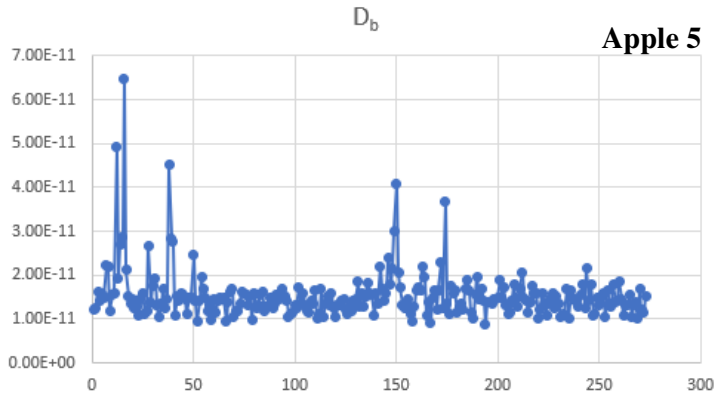

5.13 – Diffusion coefficient obtained for different apples with the classical model. The first three apples were of the same type, while apples 4 and 5 were different to the first ones, and between them.

Figure 5.13 shows that the diffusion coefficient is in the same order of magnitude for every analyzed apple, even though its behavior through the measurements is different. The average values obtained for each apple, along with their standard deviations, are shown in the following table.

Table 5.6 – Average value and standard deviation of both D_B and β obtained for five different apples.

	Average D_B	St. Dev. Of D_B	Average of β	St. Dev. Of β
Apple 1	$8.89\text{x}10^{-12}$	$2.43\text{x}10^{-12}$	0.456	0.0280
Apple 2	$1.12\text{x}10^{-11}$	$4.09\text{x}10^{-12}$	0.452	0.0263
Apple 3	$1.16\text{x}10^{-11}$	$4.97\text{x}10^{-12}$	0.460	0.0313
Apple 4	$8.89\text{x}10^{-12}$	$3.96\text{x}10^{-12}$	0.449	0.0303
Apple 5	$1.50\text{x}10^{-11}$	$5.67\text{x}10^{-12}$	0.461	0.0272

It can be seen that the values for D_B are actually not that far or different from each other, and even two different kinds of apple (apples 1 and 4), coincide in their average for D_B. The standard deviation is also more acceptable than the ones obtained for previous fruits analyzed in the past sections. Regarding the β values, they are also not very different from each other, actually, they are very close between them, even for different types of apples (apple 4 and apple 5 compared to apples 1 to 3).

There are many drawbacks, though, because even though the apples were bought on the same day, there is no way of possibly knowing how different their levels of ripeness were, for example, or if they came from the same batch, or even tree, for the apples of the same kind. These types of uncertainties can affect the obtained results, and add uncertainty to all of the analysis of this, and in general any kind of fruit, but this is out of the aim of the measurements done for this thesis.

5.2.2 Comparison between models

Both the classical (without static background) and the new (with static background) model were used to analyze the fruit in order to compare them. In the following, an example of the analysis done for one apple is shown.

Classical Model

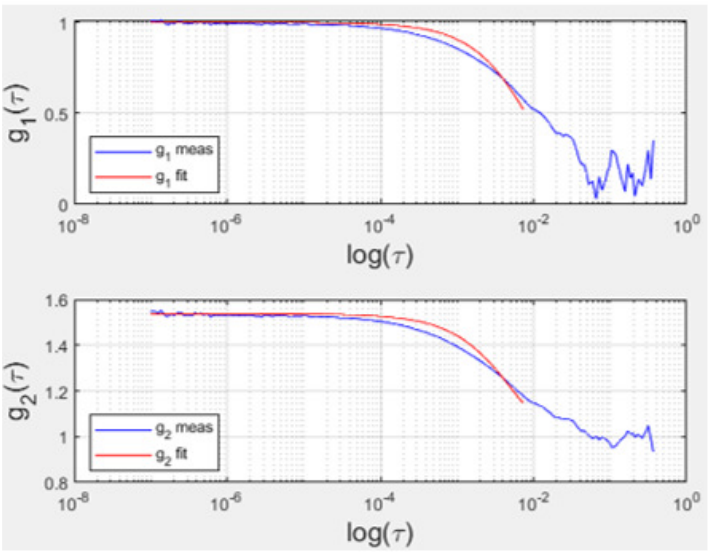

New Model $P_m = 0.025$

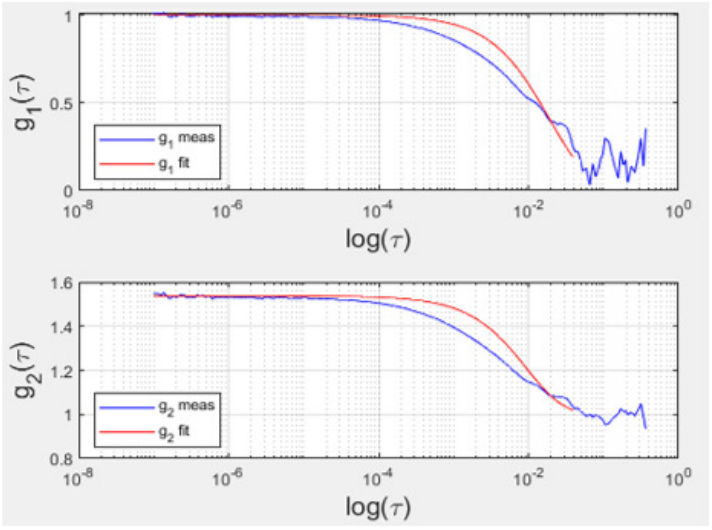

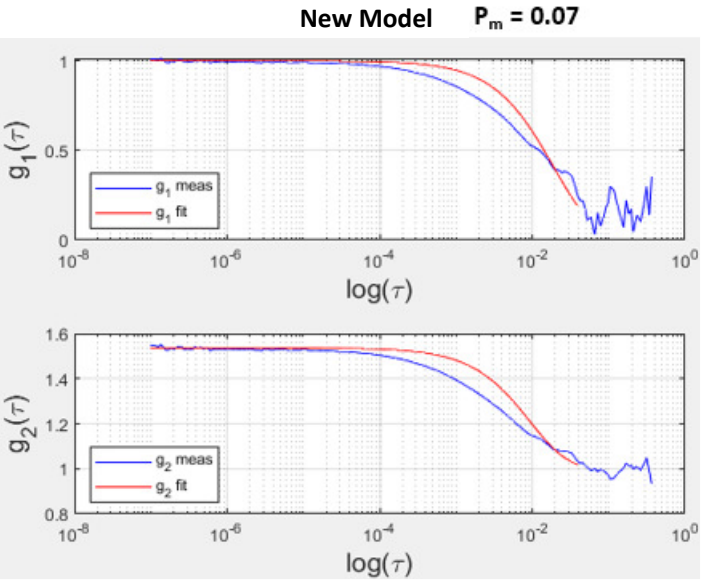

5.14 – Curves obtained for the same apple with the two different models and two different values of P_m. Their fitting is depicted in red.

There is a clear difference between the fitting curves obtained with each model. Actually, in this particular case the fitting curves obtained with the new model seem to be worse than the ones made with the classical media model. But, in general, as it has been mentioned here before, this fitting changed constantly between different data obtained for the same fruit. Some fitted very well, while some did not fit at all, like this case depicted here.

In terms of the diffusion coefficient, the change between models can be seen in a different way, as it is shown in the next figure.

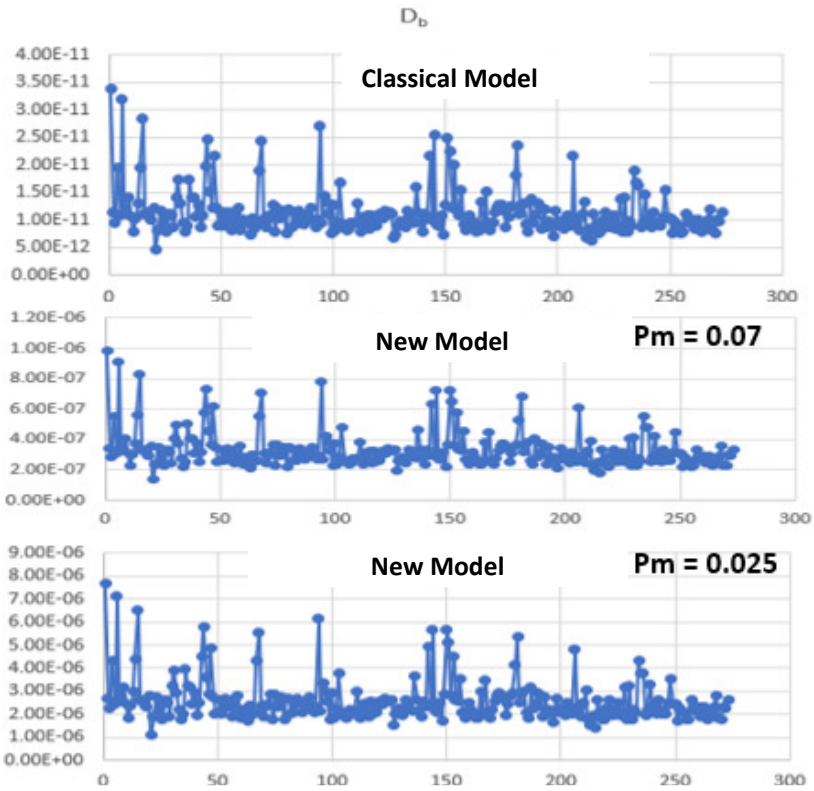

5.15– Diffusion coefficient values obtained for the same apple, but with the two different models and also two different values for P_m in the new model case.

Figure 5.15 depicts clearly that the behavior in the diffusion coefficient remains exactly the same between models, but its value changes. Actually, it can be seen that it changes in the same manner as when the value of P_m is changed. In this case, when the semi-infinite homogeneous model is used, the diffusion coefficient has its lowest value, and it increases when the static background model is used, and when P_m is changed. Besides this, there are no further changes that can be observed between the two models.

Chapter 6
Conclusions and Future Perspectives

There were two main objectives for this thesis work. The first one, which was to study the results obtained with the hybrid device for fruit, was achieved, but it may not be satisfactory due to the low reproducibility of the obtained results. This may be due to the many different factors revolving around the utilized fruit. For example, different levels of ripeness in the fruit may greatly affect the outcome of the results. Factors like the texture and thickness of the peel, the internal (and usually inhomogeneous) structure of the fruit, the amount of juice it may have, may influence the measurements. Even the position of the probe when put on each fruit may affect the outcome due to the heterogeneous and curved surface of the media.

A more controlled environment where these conditions are monitored more closely may improve the work done here, or also experimenting with different interfiber distances could improve the quality of the results. In the future, all these conditions may be studied better in order to improve the outcome of the results.

This is just an initial exploration of what can be done by studying fruits with this device, so it serves well as a parting point from which a lot can be built upon and improved so that the results can be more consistent in the future. More fruit needs to be studied to be able to reach more conclusive results.

Regarding the second objective of this thesis, which was to compare the static background model with the already used semi-infinite homogeneous media model, it can be considered a success. Both models work and fit the data well, or at least in a similar manner. Even though there is no considerable improvement in the reproducibility of the results obtained with the two models, what changes the most is the value of the obtained diffusion coefficient. This is important, and the reason behind it may as well be interesting to research in the future, as this can lead to further find or define the best method to calculate said coefficient.

Summarizing, the results are not the desired ones, but it is because of this that there is still much work and improvements to be done in the future, and this thesis may conclude on that note, with a wide, open path laid out ahead of it.

Bibliography

[1] Turgut Durduran and Arjun G. Yodh. Diffuse correlation spectroscopy for non-invasive, micro-vascular cerebral blood flow measurement. *NeuroImage*, 85:51–63, 2014.

[2] Robert C. Tasker and David K. Menon. Critical Care and the Brain. *JAMA*, 315(8):749–750, 02 2016.

[3] Mamadou Diop, Kyle Verdecchia, Ting-Yim Lee, and Keith St Lawrence. Calibration of diffuse correlation spectroscopy with a time resolved near-infrared technique to yield absolute cerebral blood flow measurements. *Biomed. Opt. Express*, 2(7):2068–2081, Jul 2011.

[4] Rath G. Bithal P. and Mahajan C. Advances in neuromonitoring. *Anesth. Essays Res.* 7, 2013.

[5] Erin M. Buckley, Ashwin B. Parthasarathy, P. Ellen Grant, Arjun G. Yodh, and Maria Angela Franceschini. Diffuse correlation spectroscopy for measurement of cerebral blood flow: future prospects. *Neurophotonics*, 1(1):1 – 7, 2014.

[6] Martina Giovannella, Davide Contini, Marco Pagliazzi, Antonio Pifferi, Lorenzo Spinelli, Rainer Erdmann, Roger Donat, Ignacio Rocchetti, Matthias Rehberger, Niels König, Robert H. Schmitt, Alessandro Torricelli, Turgut Durduran, and Udo M. Weigel. BabyLux device: a diffuse optical system integrating diffuse correlation spectroscopy and time-resolved near-infrared spectroscopy for the neuromonitoring of the premature newborn brain. *Neurophotonics*, 6(2):1 – 15, 2019.

[7] Agnese De Carli, Björn Andresen, Martina Giovannella, Turgut Durduran, Davide Contini, Lorenzo Spinelli, Udo Michael Weigel, Sofia Passera, Nicola Pesenti, Fabio Mosca, Alessandro Torricelli, Monica Fumagalli, and Gorm Greisen. Cerebral oxygenation and blood flow in term infants during postnatal transition: Babylux project. *Archives of Disease in Childhood - Fetal and Neonatal Edition*, 104(6):F648–F653, 2019.

[8] Michele Lacerenza, Mauro Buttafava, Marco Renna, Alberto Dalla Mora, Lorenzo Spinelli, Franco Zappa, Antonio Pifferi, Alessandro Torricelli, Alberto Tosi, and Davide Contini. Wearable and wireless time-domain near-infrared spectroscopy system for brain and muscle hemodynamic monitoring. *Biomed. Opt. Express*, 11(10):5934–5949, Oct 2020.

[9] Marco Ferrari and Valentina Quaresima. A brief review on the history of human functional near-infrared spectroscopy (fnirs) development and fields of application. *NeuroImage*, 63(2):921–935, 2012.

[10] Alessandro Luberto. Design, development and characterization of a Diffuse Correlation Spectroscopy system for microvasculature blood flow measurements. *Master's Degree Thesis,* Politecnico di Milano, 2020.

[11] Ilijana Ljevaja. Optimization of a Hybrid Time-resolved Reflectance Spectroscopy and Diffuse Correlation Spectroscopy System for Measurements of Tissue Hemodynamics In Vivo. *Master's Degree Thesis*, Politecnico di Milano, 2021.

[12] Alessandro Torricelli, Davide Contini, Antonio Pifferi, Matteo Caffini, Rebecca Re, Lucia Zucchelli, and Lorenzo Spinelli. Time domain functional nirs imaging for human brain mapping. *NeuroImage*, 85:28–50, 2014.

[13] Sergio Fantini and Angelo Sassaroli. Near-infrared optical mammography for breast cancer detection with intrinsic contrast. *Annals of Biomedical Engineering*, February 2012.

[14] J.M. Warwick. Imaging of brain function using spect. metab brain dis. *Metabolic Brain Disease volume*, pages 113–123, 2004.

[15] Fernando Calamante, David L. Thomas, Gaby S. Pell, Jonna Wiersma, and Robert Turner. Measuring cerebral blood flow using magnetic resonance imaging techniques. *Journal of Cerebral Blood Flow & Metabolism*, 19(7):701–735, 1999.

[16] Fabrizio Martelli, Samuele Del Bianco, Andrea Ismaelli, and Giovanni Zaccanti. *Light Propagation through Biological Tissue and Other Diffusive Media - Theory, Solutions and Software*. SPIE, Bellingham, Washington, USA, 2010.

[17] Lihong V. Wang and N.J. Hsin-i Wu. Hoboken. *Biomedical optics: principles and imaging*. Hoboken, N.J.: Wiley-Interscience., 2007.

[18] Markolf H. Niemz. *Laser-Tissue Interactions*. Springer, Berlin, Heidelberg, 2007.

[19] Hecht, E. (2002). *Optics*. Reading, Mass: Addison-Wesley.

[20] M. Alonso and E.J. Finn. *Fundamental University Physics Volume 1, Mechanics*. Addison-Wesley series in physics. Addison-Wesley Publishing Company, 1967.

[21] *Light Scattering*. PhysicsOpenLab. (2019, July 10). https://physicsopenlab.org/2019/07/10/light-scattering/.

[22] Irina Sokolik. (2019). *Rayleigh Scattering. Scattering and Absorption by Aerosols and Clouds.* Personal collection of Irina Sokolik, Georgia Institute of Technology, Atlanta, United States of America.

[23] Delfino, I., Lepore, M., & Esposito, R. (2020). Optical Characterization of Homogeneous and Heterogeneous Intralipid-Based Samples. *Applied Sciences*, 10(18), 6234. doi:10.3390/app10186234.

[24] Ntziachristos V. Going deeper than microscopy: the optical imaging frontier in biology. *Nature Methods*. 2010 Aug;7(8):603-614. DOI: 10.1038/nmeth.1483.

[25] Alessandro Torricelli, Antonio Pifferi, Lorenzo Spinelli, Rinaldo Cubeddu, Fabrizio Martelli, Samuele Del Bianco, and Giovanni Zaccanti. Time-resolved reflectance at null source-detector separation: Improving contrast and resolution in diffuse optical imaging. *Phys. Rev. Lett*., 95:078101, Aug 2005.

[26] Chandrasekhar, S. (1960). *Radiative transfer*. New York: Dover Publications.

[27] R. A. J. Groenhuis, H. A. Ferwerda, and J. J. Ten Bosch. Scattering and absorption of turbid materials determined from reflection measurements. 1: Theory. *Appl. Opt*., 22(16):2456–2462, Aug 1983.

[28] Daniele Contini, Fabrizio Martelli, and Giovanni Zaccanti. Photon migration through a turbid slab described by a model based on diffusion approximation. I. theory. *Appl. Opt*., 36(19):4587–4599, Jul 1997.

[29] Joseph W. Goodman. Statistical properties of laser speckle patterns. In *Laser speckle and related phenomena*, pages 9–75. Springer, 1975.

[30] Joseph W. Goodman. *Speckle phenomena in optics: theory and applications*. Roberts and Company Publishers, 2007.

[31] Joseph W. Goodman. *Some fundamental properties of speckle*. JOSA, 66(11):1145–1150, 1976.

[32] Markus Ninck, Markus Untenberger, and Thomas Gisler. Diffusingwave spectroscopy with dynamic contrast variation: disentangling the effects of blood flow and extravascular tissue shearing on signals from deep tissue. *Biomed. Opt. Express*, 1(5):1502–1513, Dec 2010.

[33] Boas D. A. PhD thesis. *Diffuse photon probes of structural and dynamical properties of turbid media: theory and biomedical applications*. University of Pennsylvania, 1996.

[34] P.-A. Lemieux and D. J. Durian. Investigating non-gaussian scattering processes by using nth-order intensity correlation functions. *J. Opt. Soc. Am.* A, 16(7):1651–1664, Jul 1999.

[35] Chao Zhou. PhD thesis. *In-vivo optical imaging and spectroscopy of cerebral hemodynamics*. University of Pennsylvania,2007.

[36] T Durduran, R Choe, W B Baker, and A G Yodh. Diffuse optics for tissue monitoring and tomography. *Reports on Progress in Physics*, 73(7):076701, jun 2010.

[37] A. Einstein. *Investigations on the Theory of the Brownian Movement*. Dover Books on Physics Series. Dover Publications, 1956.

[38] Edgar Aranda-Michel. (2014). *A look into mean squared displacement* [Video]. https://www.youtube.com/watch?v=yZ7zHg7goBc&ab_channel=ES.333

[39] David A. Boas, Sava Sakadžic, Juliette J. Selb, Parisa Farzam, Maria Angela Franceschini, and Stefan A. Carp. Establishing the diffuse correlation spectroscopy signal relationship with blood flow. *Neurophotonics*, 3(3):1 – 9, 2016.

[40] D. A. Boas, L. E. Campbell, and A. G. Yodh. Scattering and imaging with diffusing temporal field correlations. *Phys. Rev. Lett*., 75:1855– 1858, Aug 1995.

[41] Binzoni, Tiziano & Liemert, André & Kienle, Alwin & Martelli, Fabrizio. (2017). Derivation of the correlation diffusion equation with static background and analytical solutions. *Applied Optics*. 56. 795. 10.1364/AO.56.000795.

[42] Caterina Amendola, Michele Lacerenza, Mauro Buttafava, Alberto Tosi, Lorenzo Spinelli, Davide Contini, and Alessandro Torricelli. A compact multi-distance dcs and time domain nirs hybrid system for hemodynamic and metabolic measurements. *Sensors*, 21(3), 2021.

[43] C. Jakob, A. Th. Schwarzbacher, B. Hoppe, and R. Peters. The development of a digital multichannel correlator system for light scattering experiments. In *2006 IET Irish Signals and Systems Conference*, pages 99–103, 2006.

[44] Rainer Peters. *Multiple Tau Digital Real Time Correlator*. ALV GmbH, Siemensstrase 4, D-63225 Langen / Germany, 2013.

[45] Wei Liu, Jin Shen, and Xianming Sun. Design of multiple-tau photon correlation system implemented by fpga. In *2008 International Conference on Embedded Software and Systems*, pages 410–414, 2008.